https://doi.org/10.5194/egusphere-2026-4847
Preprint. Discussion started: 24 August 2026

A process-informed deep learning biosphere model for ecosystem carbon flux partitioning and beyond

Theo Glauch[1], Marcia J. Kroker[2], Sanam N. Vardag[2,5], Santiago Botía[4], André Butz[2,5,6], and Julia Marshall[1,3]

[1]Deutsches Zentrum für Luft- und Raumfahrt, Institut für Physik der Atmosphäre, Oberpfaffenhofen, Germany
[2]Heidelberg University, Institute of Environmental Physics, Heidelberg, Germany
[3]Leipziger Institut für Meteorologie, Universität Leipzig, Leipzig, Germany
[4]Max Planck Institute for Biogeochemistry, Jena, Germany
[5]Heidelberg University, Heidelberg Center for the Environment (HCE), Heidelberg, Germany
[6]Interdisciplinary Center for Scientific Computing (IWR), Heidelberg University, Heidelberg, Germany

Correspondence: Theo Glauch (theo.glauch@dlr.de)

Abstract. Ecosystems exchange carbon dioxide with the atmosphere through photosynthesis, which removes carbon dioxide, and respiration, which releases it. Eddy covariance flux towers measure only the net ecosystem exchange (NEE), which must be partitioned into gross primary production (GPP) and ecosystem respiration (R_{eco}) to understand ecosystem carbon cycling. This partitioning problem is structurally underdetermined and is traditionally resolved by fitting simplified, pre-defined functional forms separately to daytime and nighttime data, repeatedly re-optimized in short time windows and assuming spatially homogeneous land cover within the tower footprint.

We present `pyVPRNN`, a process-informed deep learning framework that unifies partitioning, mechanistic interpretation, and spatial upscaling within a single, jointly-trained model. High-resolution Sentinel-2 satellite observations of vegetation indices and land cover are combined with half-hourly flux footprints, to train a single model that resolves heterogeneous vegetation density and mixed land-cover classes within the footprint and learns the relationships governing photosynthesis and respiration directly from data, rather than prescribing them.

Applied to observations from 32 European eddy-covariance stations, `pyVPRNN` exceeds the performance of established daytime-based partitioning at most sites, and avoids uncertainties and biases that arise when nighttime-based partitioning is extrapolated to daytime conditions. Unlike the traditional partitionings, `pyVPRNN` provides a single, temporally consistent model rather than a sequence of independently re-fit and potentially inconsistent curves, at some cost to short-term adaptivity at frequently disturbed or managed sites. `pyVPRNN` performs particularly well at forest sites and undisturbed grasslands, and its spatiotemporal design further enables separation of the underlying ecosystem signal from footprint-driven measurement variability.

Using simulation experiments and observations from two eddy covariance sites, we further show that explainable AI techniques applied to `pyVPRNN` recover ecologically meaningful responses of photosynthesis and ecosystem respiration to environmental drivers such as temperature. Because its inputs consist solely of satellite observations, land cover, and meteorology,

https://doi.org/10.5194/egusphere-2026-4847
Preprint. Discussion started: 24 August 2026

without any footprint- or tower-specific information at inference time, the model also provides a direct route to spatial upscaling of carbon fluxes beyond the tower footprint.

`pyVPRNN` is implemented within the open-source `pyVPRM` framework, enabling convenient application and extension across sites and biomes.

1 Introduction

The eddy covariance method is a well-established approach for measuring the exchange of carbon dioxide between the terrestrial biosphere and the atmosphere (Baldocchi, 2003; Aubinet et al., 2012). It provides observations of the net ecosystem exchange (NEE) of carbon dioxide at the ecosystem scale at a high temporal resolution. The measured NEE represents a flux that is spatially averaged over the tower footprint, an area whose size, shape, and orientation vary dynamically with atmospheric turbulence and wind conditions (Schmid, 1997; Horst and Weil, 1992). Over the past decades, a growing global network of eddy covariance towers has been established to monitor carbon and energy fluxes across a wide range of ecosystems and climatic conditions (Chu et al., 2017; Keenan, 2026). Many of these stations are organized within coordinated tower networks that apply standardized data processing and quality control procedures, resulting in harmonized datasets that facilitate large-scale and comparative analyzes. Prominent examples include the global FLUXNET initiative (Pastorello et al., 2020; Baldocchi et al., 2001) as well as regional networks such as AmeriFlux (Novick et al., 2018) and the Integrated Carbon Observation System (ICOS) (Rebmann et al., 2018). In this study, we focus on data from the European ICOS network; however, the methodological framework developed here is generally applicable to any eddy covariance site worldwide.

By design, the eddy covariance technique can only measure the net exchange of carbon dioxide between ecosystems and the atmosphere. This net flux represents the balance between carbon uptake through photosynthesis, referred to as gross primary production (GPP), and carbon release through autotrophic and heterotrophic respiration, collectively referred to as ecosystem respiration (R_{eco}). By convention, carbon uptake is defined as negative, such that

$$\mathrm{NEE} = -\mathrm{GPP} + R_{\mathrm{eco}} \tag{1}$$

where both GPP and R_{eco} are expressed as positive quantities. Estimating GPP and R_{eco} from net ecosystem exchange measurements is essential for understanding the processes that govern ecosystem carbon cycling. Thus, flux-partitioned estimates are widely used in ecosystem and carbon cycle research, including for the parameterization and evaluation of process-based models (Lasslop et al., 2010; Bonan et al., 2014), data assimilation studies (Keenan et al., 2012), (regional) upscaling of carbon fluxes (Jung et al., 2020; Glauch et al., 2025), and remote-sensing-based estimates of photosynthesis (Running et al., 2004; Guanter et al., 2014).

Since neither GPP nor R_{eco} can be measured directly by the eddy covariance method, partitioning algorithms are required to separate the observed NEE into these two components. Two approaches are widely used for this purpose: nighttime (NT)

https://doi.org/10.5194/egusphere-2026-4847
Preprint. Discussion started: 24 August 2026

partitioning (Reichstein et al., 2005) and daytime (DT) partitioning (Lasslop et al., 2010). Both methods are routinely applied in the standard processing pipelines of modern eddy covariance datasets and are therefore included in many publicly available flux products.

Nighttime partitioning (Reichstein et al., 2005) is based on the simple ecological fact that under dark conditions, GPP essentially ceases, because photosynthesis requires light. This enables the use of nighttime measurements of net ecosystem exchange (NEE) to estimate ecosystem respiration (R_{eco}) directly, without requiring an explicit photosynthesis model. A common implementation of this approach is to fit an exponential temperature response function to nighttime NEE data in a moving time window of a few days to weeks, typically expressed by

$$R_{\mathrm{eco}}(T(t)) = R_{\mathrm{eco,ref}} \times \exp\left[E_0 \left(\frac{1}{T_{\mathrm{ref}} - T_0} - \frac{1}{T(t) - T_0}\right)\right] \tag{2}$$

where $R_{\mathrm{eco,\,ref}}$ and the activation-energy parameter E_0 are fitted parameters, $T(t)$ is the time-dependent soil or air temperature, T_{ref} is a reference temperature and and T_0 is a regression parameter. T_{ref} and T_0 are set to 15°C and -46.02°C, respectively (Lloyd and Taylor, 1994). The fitted function is then extrapolated to daytime conditions to obtain continuous estimates of ecosystem respiration, from which GPP can be inferred as the difference between NEE and R_{eco} (Reichstein et al., 2005). This method is conceptually straightforward and has been widely adopted because it avoids the need to model photosynthesis directly. However, the reliance on nighttime data also introduces important limitations and potential biases. First, nighttime turbulence is often weak and intermittent, especially under stable atmospheric conditions. This significantly reduces the number of reliable measurements and can lead to underestimation of nighttime fluxes and, hence, biased respiration estimates (Gu et al., 2005). Second, the assumption that a function based only on temperature can capture the full dynamics of respiration ignores known dependencies on other environmental drivers, such as soil moisture or vapor pressure deficit (VPD) (Atkin and Tjoelker, 2003; Reichstein et al., 2003). Third, the extrapolation of a temperature response curve from night to day implicitly assumes that respiration dynamics are the same at night and during the day, even though plant and microbial respiration can respond differently to diurnal changes in light, moisture, and temperature. Because this approach does not explicitly use daytime NEE data to inform the respiration model, it may be less effective in ecosystems where nighttime observations are sparse or exhibit large variability (Reichstein et al., 2005).

Daytime partitioning (Lasslop et al., 2010) fits a light-response model of photosynthesis together with a temperature-dependent respiration model to the observed daytime net ecosystem exchange (NEE) within a moving time window, thereby estimating GPP and R_{eco} simultaneously. A commonly used formulation expresses daytime NEE as a combination of a photosynthesis light-response curve, such as a rectangular hyperbolic response curve (Falge et al., 2001), and a temperature-dependent response for R_{eco}:

$$\mathrm{NEE}(t) = R_{\mathrm{eco}}(T) - \frac{\alpha\, P_{\max}\, I(t)}{\alpha\, I(t) + P_{\max}} \tag{3}$$

where $I(t)$ is the incident irradiance, α is the initial slope of the light response curve, $P_{\max}$ is light-saturated photosynthesis, and $R_{\mathrm{eco}}(T)$ is parameterized similarly to the nighttime-partitioning method using the Lloyd & Taylor model (Lloyd and Taylor, 1994) in Eq. 2, but using daytime data. This approach leverages the higher quality and quantity of daytime flux measurements,

https://doi.org/10.5194/egusphere-2026-4847
Preprint. Discussion started: 24 August 2026

which are less affected by low turbulence than nighttime data, and provides direct estimates of key photosynthetic parameters rather than relying on the difference between measured NEE and R_{eco} estimates extrapolated from dark periods. Because it explicitly models the response to light, daytime partitioning can capture diurnal variations in photosynthetic activity and is generally more robust in well-lit conditions. However, daytime methods carry several important caveats. First, they depend on prescribed functional forms for both photosynthesis and respiration; incorrect choices for the shape of the light-response or temperature-response curves can lead to structural model error, resulting in compensating biases between estimated GPP and R_{eco} (Lasslop et al., 2010). Second, photosynthesis is influenced by a variety of environmental controls — including VPD, water stress, and stomatal dynamics — that are not fully captured by simple light-response curves. As a result, parameter estimates may not reflect true physiological responses, but rather the combination of multiple interacting effects (Lasslop et al., 2010). Finally, because daytime partitioning fits a joint model to both photosynthesis and respiration, it is sensitive to overfitting and parameter identifiability: errors in the photosynthesis parameter estimates can be compensated for by adjustments in the respiration function, producing reasonable NEE fits but misleading estimates of the individual components.

Additionally, both daytime and nighttime partitioning approaches rely on several structural assumptions, including spatial homogeneity of vegetation density, canopy structure, and ecosystem type within the tower footprint. Eddy covariance towers are generally deployed in locations selected to maximize vegetation homogeneity within the fetch. However, truly homogeneous sites are uncommon in practice due to the intrinsic spatial variability of ecosystems and practical constraints on site selection, such as accessibility and infrastructure. As a result, flux measurements represent footprint-weighted averages over spatially heterogeneous landscapes (Chu et al., 2021, 2026). Moreover, footprint composition can differ systematically due to changes in atmospheric stability and turbulence especially between day and night. An example for this is shown in Fig. 1. Consequently, using either nighttime or daytime data to constrain the partitioning model and extrapolating to the other half of the day may introduce biases due to systematic day–night differences in the footprints. Overall, both classical approaches rely on simplifying assumptions about ecosystem processes and environmental controls, and the resulting estimates of GPP and R_{eco} can differ substantially depending on the chosen method.

In this paper, we propose a process-informed machine-learning approach that relaxes many of the assumptions underlying conventional flux partitioning methods by formulating the problem within a full-scale data-driven biosphere model. The approach combines publicly available satellite observations from Sentinel-2 and high-resolution land-cover maps with flux footprint information to explicitly account for spatial heterogeneity in vegetation density and land-cover type within the tower footprint. Because the model is learned from data using a machine-learning framework, no predefined functional forms for photosynthesis or respiration are required. Furthermore, all observations are fitted simultaneously within a single model, avoiding the sequential estimation of processes and the associated time-dependent biases.

A structurally similar approach was presented in (Tramontana et al., 2020), where meteorological variables were used in a two-branch neural network to learn the partitioning of eddy covariance fluxes into their component processes. Our approach has a similar two-branch architecuture, but adds the full range of spatial information, including satellite observations, land-cover maps, and tower footprint estimates. This allows the model to explicitly account for heterogeneity, which is not resolved in approaches relying solely on meteorological inputs.

https://doi.org/10.5194/egusphere-2026-4847
Preprint. Discussion started: 24 August 2026

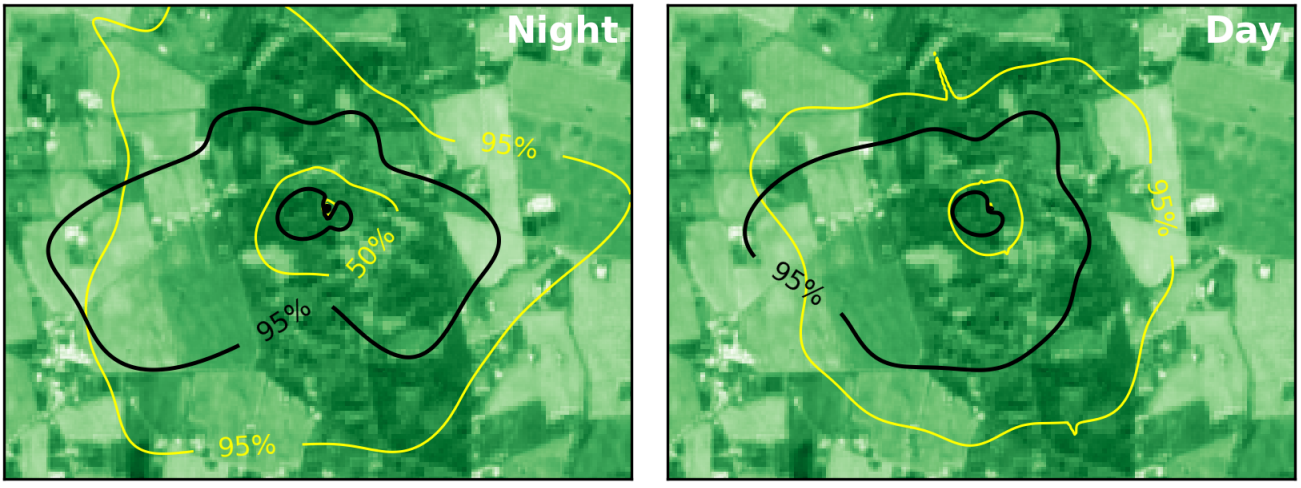

Figure 1. Daytime and nighttime aggregated flux footprints at the DK-Sor eddy-covariance tower for August 2023, estimated with the FFP footprint model (Sect. 2.3). Contours indicate 50% and 95% cumulative footprint contribution. Black contours show the footprint aggregated over only the highest-quality observations (NEE_VUT_REF_QC = 0); yellow contours show the footprint aggregated over all remaining (lower-quality) half-hours. The background shows the enhanced vegetation index (EVI) for mid-August 2023 (Sect. 2.1).

Conceptually, our approach follows the logic of the measurements at the tower site. Using localized satellite observations, land-cover information, and meteorological drivers, the model produces spatially resolved estimates of GPP and R_{eco}. These high-resolution flux estimates are then aggregated using the time-dependent tower footprint to obtain a footprint-weighted GPP and R_{eco}, which together produce the observed net ecosystem exchange measured at the tower.

Because our framework – `pyVPRNN` – represents a complete data-driven biosphere model, it can be used not only for flux partitioning but also to investigate the dependence of GPP and R_{eco} on meteorological drivers, and to upscale carbon fluxes to ecosystems with similar characteristics. Since the same model structure supports these three applications — partitioning, process interpretation, and spatial upscaling – we refer to the framework as a unified approach.

The paper is structured as follows. Section 2 describes the spatiotemporal input data, including satellite observations, land-cover maps, and the implementation of the flux footprint. Section 3.1 introduces the neural-network architecture and the construction of the training dataset. In Section 4, we present a simulation study demonstrating the applicability of the approach. Section 5 presents the results of the flux partitioning for the ICOS sites. These results are discussed in Section 6, followed by a summary and outlook in Sect. 7.

https://doi.org/10.5194/egusphere-2026-4847
Preprint. Discussion started: 24 August 2026

2 Spatiotemporal data

2.1 Satellite indices

To account for the spatial heterogeneity in vegetation density, we utilize satellite observations from the Copernicus Sentinel-2 mission. Sentinel-2 provides multispectral imagery with a revisit time of approximately five days for any given location and captures data in 13 spectral bands ranging from the visible to the shortwave infrared region at spatial resolutions of 10, 20, and 60 m (Drusch et al., 2012). These bands can be combined to derive information on vegetation density, health, canopy structure, and water stress. Commonly used vegetation indices include the Enhanced Vegetation Index (EVI) (Jiang et al., 2008), the Normalized Difference Red Edge index (NDRE) (Gitelson et al., 2005), and near-infrared reflectance of vegetation (NIRv) (Badgley et al., 2017), which differ in their spectral sensitivity to chlorophyll content, canopy structure, and biomass. The Land Surface Water Index (LSWI) (Gao, 1996), in contrast, is primarily sensitive to canopy water content and soil moisture, providing complementary information to the vegetation indices. All indices are derived from Sentinel-2 bands at their native spatial resolutions (10 m for NIRv; 10–20 m for EVI, NDRE, and LSWI) and resampled to a common 10 m grid prior to analysis.

To construct a consistent time series, we build spatiotemporal data cubes, masking out all observations lacking a reliable vegetation signal (i.e. retaining only pixels with flags 4 or 5 in the Sentinel-2 Scene Classification Layer, SCL). For each spatial pixel in the data cube, the temporal sequence is interpolated using a Kalman filter (Hird and McDermid, 2009) to estimate continuous daily values of the vegetation indices using the implementation in the `pykalman` package. Figures 2 and 3 illustrate this for the deciduous forest at the ICOS station Soroe (DK-Sor) (Ibrom et al., 2026) and the evergreen needle-leaf forest at the ICOS station Svartberget (SE-Svb) (Peichl et al., 2026), respectively. These two sites will be discussed in some detail throughout this paper. Instead of the standard EVI, the EVI2 index (Jiang et al., 2008) is shown, which provides similar information but does not rely on the blue spectral band, thus reducing sensitivity to atmospheric scattering and surface reflectance variability.

As expected, DK-Sor shows a much stronger seasonal variability than SE-Svb. Amongst the vegetation indices, NIRv, EVI2 and NDRE show a very similar time evolution, indicating that they contain much the same information.

Repeating the Kalman filter procedure for every pixel in the region of interest yields a data cube with interpolated satellite indices for each day between the first and last satellite observation. An example snapshot of interpolated (cloud-free) NIRv and LSWI maps for one day at both sites is shown in the bottom panels of Figs. 2 and 3.

2.2 Land-cover maps

Heterogeneity can result not only from variations in the vegetation density, it is not unsual that different land-cover classes contribute to the signal measured at a tower. To disentangle these signals, we utilize high-resolution land-cover maps that enable GPP and R_{eco} to be modeled as functions of land-cover class.

Although land-cover products with 10-m spatial resolution, such as ESA WorldCover (Zanaga et al., 2022) or the Copernicus Dynamic Land Cover dataset (Copernicus Land Monitoring Service, 2025), are increasingly used, they typically do not distin-

https://doi.org/10.5194/egusphere-2026-4847
Preprint. Discussion started: 24 August 2026

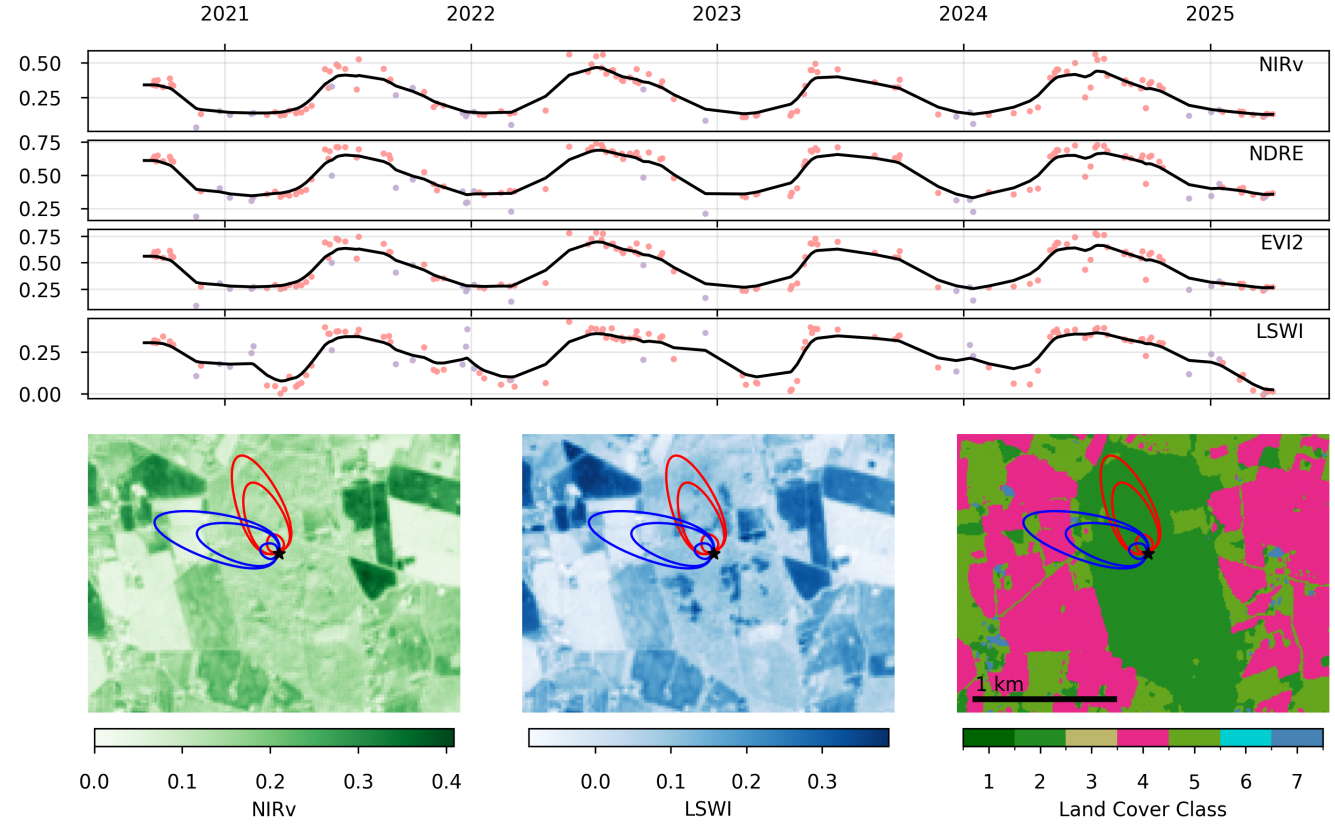

Figure 2. Overview of site characteristics at the eddy covariance station DK-Sor (Ibrom et al., 2026). The top panels illustrates temporal smoothing of the satellite-derived vegetation indices from 2020 to 2025 at the tower location. Individual Sentinel-2 observations are displayed as dots, colored according to the scene classification (SCL). Only observations classified as SCL 4 (vegetated, red) and SCL 5 (non-vegetated, blue) are included. The black solid lines indicate the daily time series reconstructed using Kalman filter interpolation. The bottom panels show spatial snapshots of NIRv (left), LSWI (middle), and land-cover class (right) for 6 March 2026. Flux footprints are shown for two time steps, 2022-05-28 15:30 UTC (blue) and 2022-03-06 17:00 UTC (red), with the 50%, 90%, and 95% cumulative contribution contours plotted. Land-cover classes are defined according to Table 1.

https://doi.org/10.5194/egusphere-2026-4847
Preprint. Discussion started: 24 August 2026

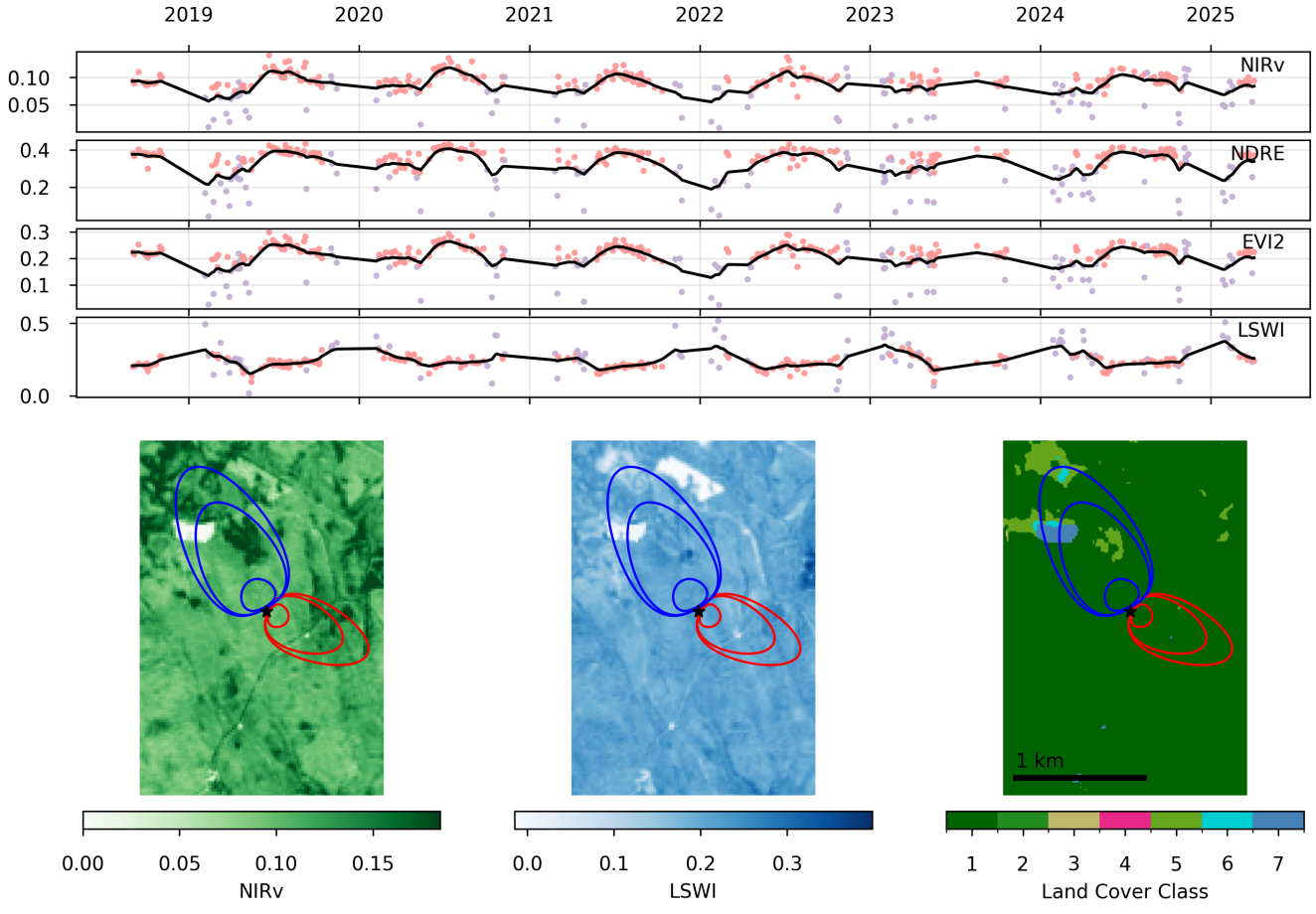

Figure 3. Overview of site characteristics at the eddy covariance station SE-Svb (Peichl et al., 2026). The top panels illustrates temporal smoothing of the satellite-derived vegetation indices from 2018 to 2025 at the tower location. Individual Sentinel-2 observations are displayed as dots, colored according to the scene classification (SCL). Only observations classified as SCL 4 (vegetated, red) and SCL 5 (non-vegetated, blue) are included. The black solid lines indicate the daily time series reconstructed using Kalman filter interpolation. The bottom panels show spatial snapshots of NIRv (left), LSWI (middle), and land-cover class (right) for 5 November 2019. Flux footprints are shown for two time steps, 2019-11-05 02:30 UTC (blue) and 2019-08-11 23:30 UTC (red), with the 50%, 90%, and 95% cumulative contribution contours plotted. Land-cover classes are defined according to Table 1.

https://doi.org/10.5194/egusphere-2026-4847
Preprint. Discussion started: 24 August 2026

guish between different forest types. To address this limitation, we construct a hybrid dataset that combines the detailed forest classification of the 100-m Copernicus Dynamic Land Cover maps (Copernicus Land Monitoring Service, 2019) with the 10-m spatial resolution of ESA WorldCover. This approach allows us to represent forest type while retaining high spatial resolution, and provides the flexibility to update the land-cover information when more detailed 10-m products become available.

For modeling purposes, we aggregate the 11 land-cover classes from ESA WorldCover into six categories: forest, shrubland, cropland, grassland, wetland, and non-vegetated. The forest class is further subdivided into evergreen and deciduous forests using the forest-type information from the 100-m Copernicus Dynamic Land Cover map. The mapping details are provided in Table 1. Using the `pyVPRM` (Glauch et al., 2025) and `xESMF` packages (Zhuang et al., 2023), we regrid the land-cover map to the resolution of the Sentinel-2 data, producing a fractional representation of each land-cover class for every pixel. Figures 2 and 3 also illustrate the dominant land-cover class for each satellite pixel near the stations DK-Sor and SE-Svb (lower right panels).

Table 1. Mapping from ESA WorldCover and Copernics Dynamic Land Cover classes to internal `pyVPRNN` classes.

Internal Class	pyVPRNN Class	ESA WorldCover Class Numbers	Copernics Dynamic Land Cover Class Numbers
Evergreen Forest	1	10	111, 112, 121, 122
Deciduous Forest	2	10	113, 114, 123, 124
Shrubland	3	20	–
Grassland	5	30	–
Cropland	4	40	–
Wetland	6	90	–
Other	7	50, 60, 70, 80, 95, 100	–

2.3 Flux footprints

As illustrated in Figs. 2 and 3, the land cover surrounding an eddy covariance tower is often heterogeneous. Even within a single land-cover class, vegetation properties may vary substantially due to differences in canopy density, vegetation health, water availability, or land management. The flux measured by an eddy covariance tower therefore originates from an upwind source area, commonly referred to as the flux footprint. The location and extent of this footprint depend on the prevailing meteorological conditions, including wind speed, wind direction, and atmospheric stability. Consequently, temporal changes in the footprint lead to varying contributions from different parts of the surrounding landscape. This effect is illustrated for the sites SE-Svb and DK-Sor in the lower panels of Figs. 3 and 2, respectively.

Several methods have been developed to estimate flux footprints; comprehensive overviews are given by Vesala et al. (2008) and Leclerc and Foken (2014). Because this study requires the calculation of two-dimensional half-hourly footprints for multiple sites over several years, we employ a computationally efficient footprint model that depends on only a small number of meteorological variables. Such models generally assume horizontally homogeneous terrain and either derive analytical expressions for the footprint (Kormann and Meixner, 2001; Schmid, 1994) or parameterize more complex numerical models (Kljun

https://doi.org/10.5194/egusphere-2026-4847
Preprint. Discussion started: 24 August 2026

et al., 2015b; Hsieh et al., 2000). Their accuracy is therefore expected to decrease under conditions that deviate substantially from those used during model development.

We adopt the parameterized footprint model of Kljun et al. (2015b), hereafter referred to as the FFP model. It was developed for a comparatively wide range of atmospheric conditions and has been shown to perform favorably compared with alternative analytical footprint models (Heidbach et al., 2017). Nevertheless, the modular design of `pyVPRM`/`pyVPRNN` allows alternative footprint models to be incorporated with minimal modifications.

The FFP model is fully determined by the measurement height above the zero-plane displacement, z_m, the mean wind speed u, the Monin–Obukhov length L (or equivalently the stability parameter z/L), the friction velocity u^*, the standard deviation of the lateral wind component σ_v, and the boundary layer height h. The complete formulation is given by Kljun et al. (2015b) and reproduced in Appendix A1; only a brief overview is presented here.

The footprint is defined on a Cartesian coordinate system with the x axis aligned with the mean wind direction and the y axis perpendicular to it. The origin is located at the tower, while the surface corresponds to the zero-plane displacement height. The footprint function $\phi(x,y)$ is expressed as the product of an along-wind distribution $\overline{f^y}(x)$ and a crosswind dispersion term $D_y(x,y)$,

$$\phi(x,y) = D_y(x,y)\overline{f^y}(x). \tag{4}$$

The crosswind dispersion is represented by a Gaussian distribution,

$$D_y(x,y) = \frac{1}{\sqrt{2\pi}\sigma_y}\exp\left[-\frac{y^2}{2\sigma_y^2}\right], \tag{5}$$

where the standard deviation σ_y depends on the meteorological input variables. The along-wind distribution is given by

$$\overline{f^y}(x) = a(X^*(x)-d)^b \exp\left[-\frac{c}{X^*(x)-d}\right]\frac{(1-\frac{z_m}{h})u^*}{z_m\, u\, k}, \tag{6}$$

where X^* denotes the dimensionless upwind distance and $k = 0.4$ is the von Kármán constant. The resulting footprint exhibits a pronounced maximum close to the tower and an exponentially decaying tail in the upwind direction. Examples are shown in the lower panels of Fig. 3. Stable atmospheric conditions generally produce elongated and narrow footprints, whereas unstable conditions lead to shorter and wider source areas. Likewise, towers mounted higher above the canopy integrate fluxes over a larger spatial extent.

The FFP model is recommended for atmospheric stability parameters satisfying $-15.5 \leq z/L$ (Kljun et al., 2015b), and its parameters were calibrated primarily for friction velocities between approximately 0.2 and $0.5\,\mathrm{m\,s^{-1}}$. In this study, footprints are nevertheless computed outside these recommended ranges. Although their quantitative accuracy is expected to decrease, they still provide useful information on the dominant source area and, in particular, on the effect of changing wind direction. As discussed in Sect. 3.2, observations with insufficient turbulence, as indicated by low u^* values, are excluded from neural-network training based on the ICOS quality flags (Pastorello et al., 2020), but are retained during evaluation.

Not all meteorological variables required by the FFP model are available for every station in the ICOS Level 2 release (RI et al., 2025). Sites lacking measurements of σ_v are therefore excluded from the analysis. Boundary layer height h is also

https://doi.org/10.5194/egusphere-2026-4847
Preprint. Discussion started: 24 August 2026

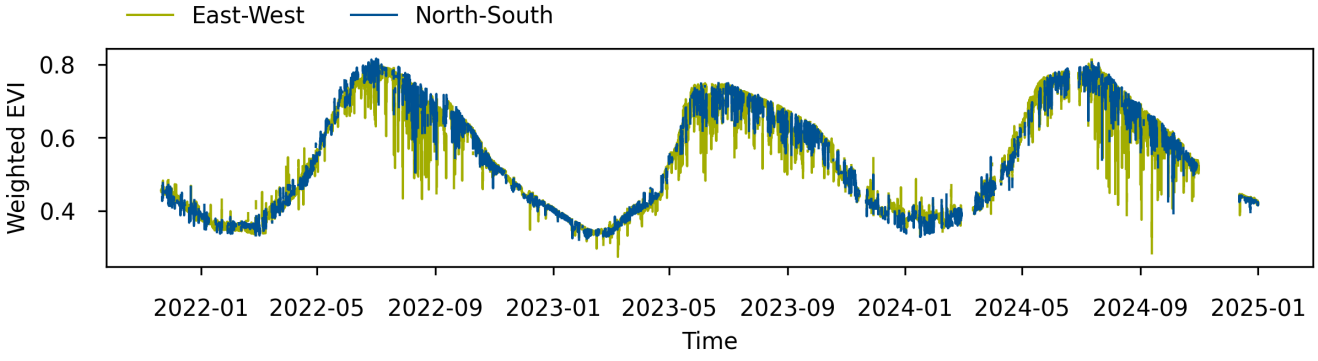

Figure 4. Footprint-weighted integral of LSWI for eddy covariance station DK-Sor. The data are separated into two groups based on the wind direction, blue dots indicate wind from the northern half of the domain, red dots indicate wind from the southern half. UUUUPDATE. Also check that main text is consistent.

unavailable for many stations. However, Heidbach et al. (2017) reported that varying h between 500 and 2000 m changed the integrated FFP fluxes by less than 1 % at their study site. Following their recommendation, we therefore assume a constant value of $h = 1000\,\mathrm{m}$ whenever boundary layer height observations are unavailable. Alternatively, boundary layer heights could be obtained from ERA5 (Muñoz-Sabater et al., 2021), but previous studies have demonstrated considerable uncertainties in ERA5 boundary layer height estimates (Xi et al., 2024; Alladi et al., 2026). Appendix A2 describes the determination of the measurement height above the zero-plane displacement.

Before computing the footprints, we estimate their characteristic spatial extent in order to determine the computational domain. The distance x_R enclosing a fraction R of the measured flux is given by

$$x_R = \left(\frac{-c}{ln(R)} + d\right) z_m \frac{\frac{u}{u^*}k}{(1 - \frac{z_m}{h})}. \tag{7}$$

The computational domain is chosen to be twice the size corresponding to the 95 % cumulative source area ($R = 0.95$). Footprints are initially calculated on a high-resolution grid of 1500×1500 pixels and subsequently aggregated to the satellite grid using `xESMF` (Zhuang et al., 2023). Details of the regridding procedure are provided in Appendix A3.

An intuitive illustration of the influence of flux footprints can be obtained by calculating footprint-weighted satellite indices, although within the neural network itself the footprint weighting is applied at a later stage. Figure 4 shows the footprint-weighted EVI time series for the DK-Sor site. Clear time-dependent effects are visible, differing systematically depending on whether the wind is blowing along the north–south or east–west axis — the major axis of landscape asymmetry at this site (Fig. 2). Incorporating footprint information therefore allows the neural network to account for spatial heterogeneity in the surrounding landscape.

https://doi.org/10.5194/egusphere-2026-4847
Preprint. Discussion started: 24 August 2026

3 Neural-network model

Machine learning approaches have become a popular tool for modeling biospheric carbon fluxes at high spatiotemporal resolution. Models have been developed for both flux partitioning (Tramontana et al., 2020; Ranjbar et al., 2026) and upscaling (Jung et al., 2020; Gaber et al., 2024; Zhu et al., 2024; Papale and Valentini, 2003). Compared to traditional parametric approaches, neural networks have the advantage that they can learn the relationships between input variables and target fluxes directly from data, without requiring explicit functional forms.

Using eddy covariance stations, which typically provide half-hourly measurements, we can obtain training datasets on the order of $\mathcal{O}(10^5)$ observations per year before quality filtering and data selection, which is sufficient for extensive neural network training. The effective dataset is even larger when considering the spatial extent and heterogeneity of the input fluxes within the tower footprint, which provide additional, though not fully independent, information.

In this work, we propose a neural-network model that maps harmonized and aligned inputs from Sentinel-2 satellite observations, high-resolution land-cover maps, meteorological data, and half-hourly flux tower footprints to GPP and R_{eco}, from which NEE can be calculated.

3.1 Model architecture

A schematic overview of the model architecture is shown in Fig.5. The model consist of two parallel branches that estimate GPP and R_{eco}, respectively. Within each branch, a sequence of 1×1 convolutional layers (Lin et al., 2013) are trained to map the input variables – meteorological drivers, satellite observations, and fractional land-cover information – stacked along the channel dimension to spatial flux maps that, by model construction, represent GPP and R_{eco}. For processing and data-handling reasons, the input is split up into static components, like land-cover maps and maximum/minimum NIRv, and dynamic satellite data, such as the time-dependend NIRv, LSWI, NDRE, and meteorological variables. The size of the input images will differ depending on the maximum extent of the tower footprint. Typical values are on the order of $O(10^2)$ x $O(10^2)$ pixels for the case of 10-m Sentinel-2 pixels, representing a quadratic region of a few kilometers around the tower location.

Meteorological inputs are available only as single values per timestep (i.e., no spatially resolved micrometeorological measurements), so these variables are broadcast across the spatial dimensions of the satellite imagery to match the resolution of the other inputs. A softmax activation function (Goodfellow et al., 2016) is applied to ensure a smooth dependence of the convolutional weights on the input features.

To relate the spatial flux estimates to eddy-covariance observations, the predicted GPP and R_{eco} flux maps are multiplied by the time-dependent, normalized tower footprint, which weights each pixel's contribution according to its influence on the flux measured at the tower (Schmid, 1997; Kljun et al., 2015a). An additional mask sets GPP and R_{eco} to zero for land-cover classes that are not associated with biogenic carbon-dioxide fluxes (e.g., water, urban surfaces).

The symmetry between the two branches is broken by imposing a day–night mask: GPP is set to zero during nighttime based on top-of-the-atmosphere incoming radiation, forcing the network to learn R_{eco} from nighttime NEE observations. During daytime, the combined contributions of GPP and R_{eco} must reproduce the observed NEE. Hence, the network has

https://doi.org/10.5194/egusphere-2026-4847
Preprint. Discussion started: 24 August 2026

some flexibility to adjust R_{eco}, but only insofar as this does not compromise the nighttime predictions. In addition, a pixel-wise mask sets fluxes from permanently non-vegetated areas to zero in both branches (No-Flux Mask).

Within each branch, the footprint-weighted flux maps are spatially summed to obtain the predicted GPP and R_{eco} at the tower location. Net ecosystem exchange is then calculated as the difference between the two fluxes, yielding the predicted NEE ($\mathrm{NEE}_{\mathrm{pred}}$), which is compared to the observations ($\mathrm{NEE}_{\mathrm{true}}$) during training.

By using 1×1 convolutions (Lin et al., 2013), the model effectively functions as a landcover-aware data-driven biosphere model, operating independently but consistently at each pixel along the channel dimension. This design makes the model agnostic to the spatial extent of the input data, allowing it to be efficiently applied to domains ranging from single pixels to larger spatial tiles. Consequently, the trained network can be used to predict GPP and R_{eco} from the respective neural network branch for similar ecosystems beyond the original tower footprint, supporting spatial upscaling of carbon flux estimates (see Fig.5).

Several model variants have been developed within the `pyVPRM` framework. The model presented in this study, together with future extensions, is available through the `pyVPRM` main repository and the accompanying examples repository [1] [2] (Glauch et al., 2025). In this work we discuss the model variant `pyVPRNN_v1`: It uses spatial maps of NDRE, LSWI, and NIRv in both branches. Meteorological inputs for this version include the site-level-measured 2-m air temperature (t2m), surface solar radiation downwards (ssrd), and relative humidity (RH) – all of which are also included in the ERA5-Land reanalysis product (Muñoz-Sabater et al., 2021). In addition volumetric soil water content in the second soil layer (swvl2; depth 7–28 cm) is directly taken from ERA5-Land. For ecosystem respiration, ssrd is excluded and the ERA5-Land near-surface soil moisture variable swvl1 (depth 0–7 cm) is used instead of swvl2, reflecting the stronger influence of top-soil conditions on microbial respiration. Both branches also receive a static input including the pixel-wise minimum and maximum NIRv over the entire study period as well as the fractional coverage of all land-cover classes listed in Tab. 1.

A summary of the network architecture and parameter counts is provided in Fig. 5 and in Tab. A1.

3.2 Input dataset

The ICOS Ecosystem network comprises eddy covariance stations distributed across Europe, covering a wide range of ecosystem types and climatic conditions. In addition to carbon flux measurements, ICOS provides high-quality meteorological observations that are processed using standardized and well-documented procedures (Rebmann et al., 2018). The consistency of the measurements and processing makes the ICOS dataset an ideal testbed for developing and evaluating the framework presented in this study.

We use the ICOS Level 2 Ecosystem release 2025-1 dataset (RI et al., 2025) and retain only stations and time periods for which all meteorological variables required for the computation of flux footprints are available. Furthermore, the analysis is restricted to evergreen needleleaf forests, deciduous broadleaf forests, and grasslands, as these ecosystem types exhibit few abrupt disturbances. Cropland sites are excluded because crop rotations and management practices introduce substantial

[1] https://github.com/tglauch/pyVPRM
[2] https://github.com/tglauch/pyVPRM_examples

https://doi.org/10.5194/egusphere-2026-4847
Preprint. Discussion started: 24 August 2026

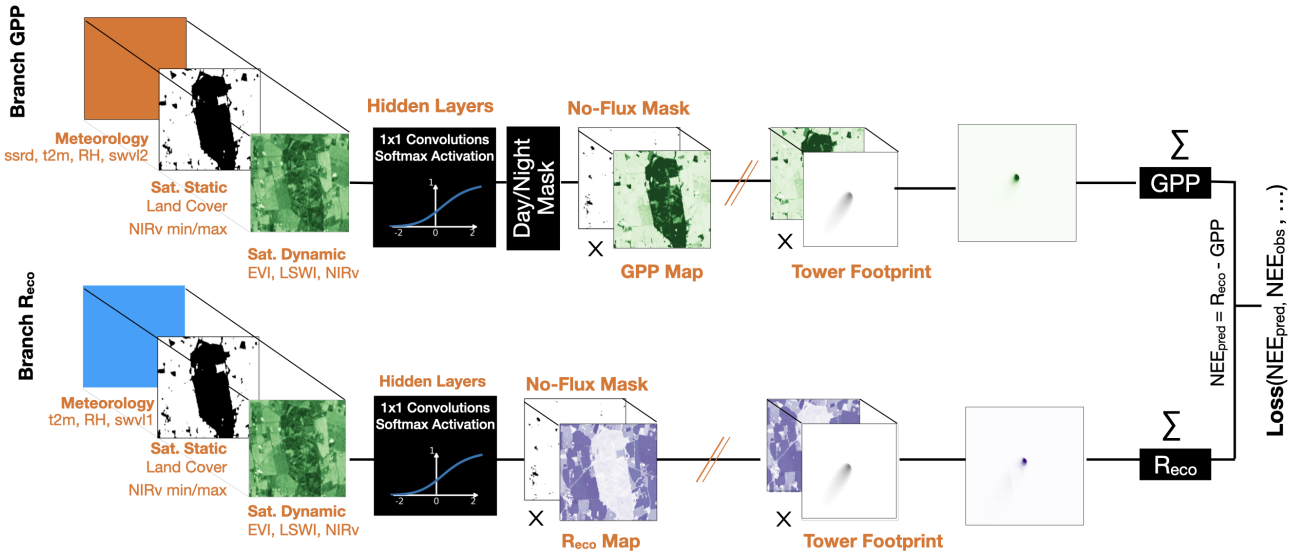

Figure 5. Schematic representation of the architecture of the neural network `pyVPRNN_v1`. The input is separated into different branches for meteorology, static satellite-based images (Sat. Static), and satellite images that vary with time (Sat. Dynamic). For the static map the fraction of deciduous forest at the site DK-Sor is shown on a color scale from high-fraction (black) to low fraction (white). The loss function will generally depend on the NEE predictions of the neural network and the true NEE measured at the tower, though other variables could also be included. In this work we use a Laplace negative log-likelihood, see Equation 8. The red lines mark where each branch is truncated for pixel-wise inference and upscaling, extracting the per-pixel GPP/Reco maps before footprint weighting and summation.

temporal changes in vegetation structure and physiology that would require additional information, such as crop calendars, to be represented adequately. Extending the framework to managed agricultural systems is therefore left for future work. Figure 6 provides an overview of the ICOS stations included in this study.

The quality of eddy covariance flux measurements depends on several factors, including atmospheric turbulence (commonly characterized by the friction velocity, u^*), carbon-dioxide storage below the canopy, and instrument performance. To avoid biases introduced by gap-filling algorithms, we restrict both training and validation to directly measured NEE observations (NEE_VUT_REF_QC = 0). This ensures that the neural network is trained exclusively on measured fluxes rather than on values that already incorporate assumptions from empirical gap-filling methods. In addition, we remove physically implausible nighttime observations, defined as periods with zero incoming shortwave radiation but negative measured NEE, corresponding to an apparent nighttime carbon sink.

The resulting training datasets contain between a few thousand and more than 50,000 observations per site, depending primarily on the length of the measurement record. An overview of the selected sites and the corresponding dataset sizes is provided in Table 2.

https://doi.org/10.5194/egusphere-2026-4847
Preprint. Discussion started: 24 August 2026

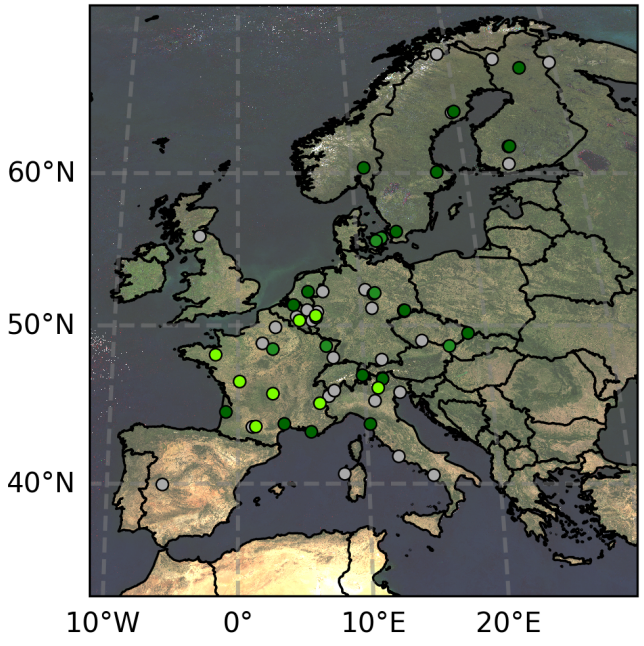

Figure 6. Map of Europe showing ICOS eddy covariance stations (Release 2025-1, Level 2 Ecosystem data (RI et al., 2025)). Stations included in this study are highlighted by vegetation type: evergreen forests (dark green), deciduous forests (medium green), and grasslands (light green). Stations from the same release with these vegetation types but excluded due to missing variables required for footprint calculations are shown in grey. The background map is based on MODIS satellite imagery.

3.3 Model training

Although the architecture of our neural network is relatively simple and does not include highly complex components, achieving convergence is non-trivial. This difficulty arises from the high degeneracy of possible daytime GPP and R_{eco} combinations that can produce the same NEE signal. In fact, we find that model simplicity is crucial for training stability. More complex architectures, such as those incorporating residual layers, tended to be less stable and harder to optimize in practice.

As loss function we use a Laplace negative log-likelihood (LNLL) with observed NEE y_i^{true} (NEE_VUT_REF) and scale parameter b_i for each of N samples in a batch,

$$\mathcal{L} = \frac{1}{N}\sum_{i=1}^{N}\left[\frac{|y_i^{\mathrm{true}} - y_i^{\mathrm{pred}}|}{b_i} + \log(2b_i)\right] \tag{8}$$

where the scale parameter b_i is derived from the flux uncertainty estimate σ_i (NEE_VUT_REF_JOINTUNC) as $b_i = \sigma_i/\sqrt{2}$, so that the implied variance $2b_i^2 = \sigma_i^2$ matches that of the Gaussian formulation. We use a Laplace likelihood because eddy-covariance random flux errors are known to be better described by a double-exponential (Laplace) than a normal distribution

https://doi.org/10.5194/egusphere-2026-4847
Preprint. Discussion started: 24 August 2026

Site	Veg.	Lat. [deg]	Lon. [deg]	Period	Datapoints	Measured	With Footprint	Training Dataset
BE-Bra	ENF	51.308	4.520	2019-12-31 – 2024-12-31	87696	36802	45577	20950
BE-Dor	GRA	50.312	4.968	2021-12-31 – 2024-12-31	52608	13652	20664	7610
CH-Dav	ENF	46.815	9.856	2018-12-31 – 2024-12-31	105216	25195	49681	10267
CZ-BK1	ENF	49.502	18.537	2021-12-31 – 2024-12-31	52608	14660	23170	6068
CZ-Lnz	DBF	48.682	16.946	2021-12-31 – 2024-12-31	52608	24086	28467	13608
DE-HoH	DBF	52.087	11.222	2018-12-31 – 2024-12-31	105216	40156	60641	22060
DE-RuR	GRA	50.622	6.304	2010-12-31 – 2024-12-31	245472	103895	129467	55763
DE-RuW	ENF	50.505	6.331	2011-12-31 – 2024-12-31	227952	64312	99005	28456
DE-Tha	ENF	50.963	13.565	2019-12-31 – 2024-12-31	87696	32684	40289	15934
DK-RCW	DBF	55.681	12.101	2022-12-31 – 2024-12-31	35088	16687	18830	9987
DK-Sor	DBF	55.486	11.645	2020-12-31 – 2024-12-31	70128	22138	29536	11744
FI-Hyy	ENF	61.847	24.295	2017-12-31 – 2024-12-31	122736	25169	50737	12105
FI-Sod	ENF	67.362	26.639	2022-12-31 – 2024-12-31	35088	8285	15665	3615
FR-Bil	ENF	44.494	-0.956	2018-12-31 – 2024-12-31	105216	40748	50765	18400
FR-CLt	GRA	45.041	6.411	2018-12-31 – 2024-12-31	105216	28606	57306	14700
FR-FBn	ENF	43.241	5.679	2021-12-31 – 2024-12-31	52608	11200	20484	5308
FR-Fon	DBF	48.476	2.780	2018-12-31 – 2024-12-31	105216	43311	50271	22819
FR-Hes	DBF	48.674	7.065	2021-12-31 – 2024-12-31	52608	17160	25145	8984
FR-Lqu	GRA	45.644	2.735	2021-12-31 – 2024-12-31	52608	10642	17979	4390
FR-Lus	GRA	46.414	0.121	2021-12-31 – 2024-12-31	52608	16173	18602	8604
FR-Mej	GRA	48.118	-1.796	2018-12-31 – 2024-12-31	105216	58575	55636	31064
FR-Pue	EBF	43.741	3.596	2020-12-31 – 2024-12-31	70128	17879	26876	8467
FR-Tou	GRA	43.573	1.375	2017-12-31 – 2024-12-31	122736	44543	66134	18758
GL-ZaH	GRA	74.473	-20.551	2020-01-01 – 2025-01-01	87696	11157	9000	3033
IT-MBo	GRA	46.015	11.046	2021-12-31 – 2024-12-31	52608	11217	20080	5192
IT-Ren	ENF	46.587	11.434	2020-12-31 – 2024-12-31	70128	10691	26150	3209
IT-SR2	ENF	43.732	10.291	2018-12-31 – 2024-12-31	105216	27757	49758	13102
NL-Loo	ENF	52.166	5.744	2022-12-31 – 2024-12-31	35088	17251	18586	10705
NO-Hur	ENF	60.372	11.079	2022-12-31 – 2024-12-31	35088	5384	13214	3181
SE-Htm	ENF	56.098	13.419	2017-12-31 – 2024-12-31	122736	48634	74949	25577
SE-Nor	ENF	60.086	17.480	2017-12-31 – 2024-12-31	122736	46057	67124	27088
SE-Svb	ENF	64.256	19.774	2018-12-31 – 2024-12-31	105216	30720	58219	15325

Table 2. Overview of the eddy covariance stations used in this study. From left to right, the table reports site name, vegetation type, geographic coordinates (latitude and longitude), ICOS data availability period, total number of data points, number of measured (not gap-filled) data points, number of data points with available footprint information, and the resulting training dataset size. Vegetation types are abbreviated as follows: ENF = evergreen needleleaf forest, EBF = evergreen broadleaf forest, DBF = deciduous broadleaf forest, and GRA = grassland. Based on data from the Ecosystem final quality (L2) product release 2025-1 (RI et al., 2025).

(Hollinger and Richardson, 2005). To avoid numerically unstable or degenerate weighting from anomalously small uncertainty estimates, σ_i is floored at $\sigma_{\min} = 0.5\ \mu\mathrm{mol\,m^{-2}\,s^{-1}}$ before conversion to b_i.

https://doi.org/10.5194/egusphere-2026-4847
Preprint. Discussion started: 24 August 2026

To discourage implausible flux values, two soft penalty terms are added to the training loss (Eq. **??**). The first penalizes individual pixel-level GPP predictions $\hat{\text{GPP}}$ exceeding a fixed ceiling $\theta_{\text{GPP}} = 40\ \mu\text{mol}\,\text{CO}_2\,\text{m}^{-2}\,\text{s}^{-1}$:

$$\mathcal{L}_{\text{GPP}} = \lambda_{\text{GPP}} \cdot \text{mean}\Big(\text{ReLU}\big(\hat{\text{GPP}} - \theta_{\text{GPP}}\big)\Big) \tag{9}$$

averaged over all pixels and samples in the batch.

The second penalty reflects the expectation that GPP and R_{eco}, accumulated over a sufficiently long period, should approximately balance – a persistent, large imbalance at a given location would imply an implausibly strong, sustained carbon source or sink, violating the assumption of an approximately closed carbon budget. We therefore accumulate the predicted daytime GPP and R_{eco} separately for each pixel over all timesteps in the batch and penalize their ratio $\hat{r}$ for exceeding a plausible maximum $r_{\max}$:

$$\mathcal{L}_{\text{ratio}} = \lambda_{\text{ratio}} \cdot \underset{\hat{r} > r_{\max}}{\text{mean}} \left(\text{ReLU}\left(\hat{r} - r_{\max}\right)\right) \tag{10}$$

Using the batch-accumulated signal rather than individual timesteps is essential here: at any single timestep GPP and R_{eco} can diverge strongly, whereas accumulating over many timesteps averages out this short-term decoupling and isolates only genuine, sustained imbalances. Both terms are added to the main loss with fixed weights $\lambda_{\text{GPP}} = \lambda_{\text{ratio}} = 10^{-4}$.

To ensure a stable training procedure, we use the Adam optimizer with an initial learning rate of 3×10^{-3} and a batch size of 64 samples. To support convergence, the learning rate is reduced by a factor of two whenever the validation loss does not improve for 10 consecutive epochs. We further apply early stopping, terminating training after 20 epochs without improvement and retaining the model state that achieved the lowest validation loss.

After training, we apply the model to all observations for which a valid footprint can be calculated, independent of quality flags. Although reapplying a model to its training data can in general lead to overfitting concerns, this is not observed here. The model is strongly regularized through its dependence on a large number of input pixels, which limits its ability to memorize specific artifacts. We validate this approach by comparing it to a 10-fold cross-validation scheme in which predictions are strictly restricted to unseen data. Across all performance metrics reported in Sect. 5, we find no meaningful differences between the two approaches. This result is further supported by smooth training and validation loss curves that show no indication of overfitting. Example curves for the sites DK-Sor and SE-Svb are shown in Fig. 7.

4 Simulation studies

As a proof of concept for the neural-network framework, we conduct a series of simulation studies. The core idea is to generate spatially explicit fields of GPP and R_{eco} using a data-driven biosphere model, aggregate these fluxes into synthetic eddy-covariance tower observations, and then attempt to recover the underlying processes using `pyVPRNN_v1`. By comparing the simulated "true" fluxes with the model estimates, we can rigorously evaluate model performance and assess its sensitivity to different process representations and parameterizations.

https://doi.org/10.5194/egusphere-2026-4847
Preprint. Discussion started: 24 August 2026

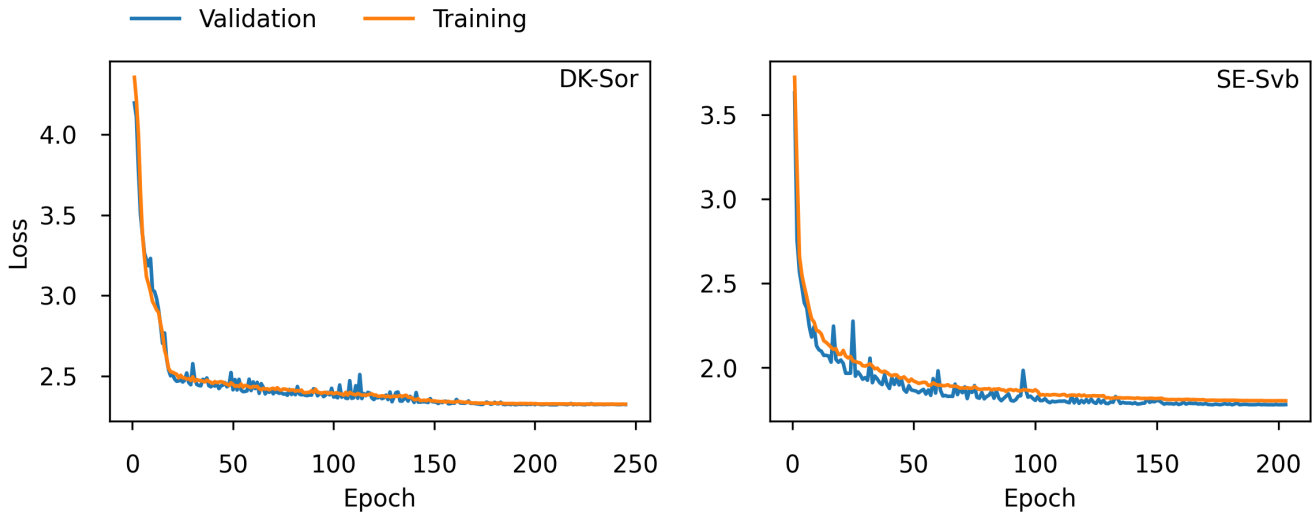

Figure 7. Training curves for the ICOS sites DK-Sor (left) and SE-Svb (right). Compared are the training and validation loss as defined in Eq. 8.

4.1 Simulation setup

For the simulations, we employ the Vegetation Photosynthesis and Respiration Model (VPRM) (Mahadevan et al., 2008; Glauch et al., 2025). VPRM is a light-use efficiency model that estimates GPP and R_{eco} using land-cover information, satellite observations (EVI, LSWI), and meteorological variables. The GPP calculation incorporates the temperature dependence of photosynthesis (T_{scale}), canopy water stress (W_{scale}), leaf age (P_{scale}), and a light-saturation term. These factors enter multiplicatively into the light-use efficiency formulation:

$$\text{GPP} = \lambda \times P_{\text{scale}} \times W_{\text{scale}} \times T_{\text{scale}} \times \frac{\text{PAR}}{1 + \text{PAR}/\text{PAR}_0} \times \text{EVI}, \tag{11}$$

where λ is the quantum efficiency, PAR_0 the saturation coefficient, and PAR the incoming photosynthetically active radiation. The temperature dependence of photosynthesis T_{scale} is represented using a modified beta-type function:

$$T_{\text{scale}} = \frac{(T - T_{\min})(T - T_{\max})}{(T - T_{\min})(T - T_{\max}) - (T - T_{\text{opt}})^2}, \tag{12}$$

parameterized by minimum, maximum, and optimal air temperatures. For ecosystem respiration, the standard VPRM model (Mahadevan et al., 2008) assumes a linear temperature dependence. In total, the model contains four free parameters per vegetation type: the quantum efficiency λ, the saturation coefficient PAR_0, and the baseline β and slope α of the respiration function. Parameter values are typically calibrated against eddy covariance observations for each vegetation type. In this study, we adopt the parameter sets reported in Glauch et al. (2025).

To evaluate whether the neural network approach can also capture more complex process relationships, we modify the standard VPRM by introducing an additional VPD dependence in GPP and an EVI-dependent scaling of R_{eco}. The VPD effect

https://doi.org/10.5194/egusphere-2026-4847
Preprint. Discussion started: 24 August 2026

on GPP is represented by the multiplicative factor $\exp(-\kappa \cdot \mathrm{VPD})$ (Medlyn et al., 2017). To account for seasonal variations in autotrophic respiration associated with vegetation dynamics (Huang et al., 2012), ecosystem respiration is modified as $R_{\mathrm{eco}} = (\alpha \cdot T + \beta)\,(\mathrm{EVI}/\mathrm{EVI}_{\mathrm{mean}})$ where $\mathrm{EVI}_{\mathrm{mean}}$ denotes the temporal mean EVI averaged over the entire region surrounding the flux tower.

To approximate realistic measurement uncertainties, a subset of the simulations includes random noise added to the simulated NEE. The noise consists of a dominant additive (absolute) component and an additional multiplicative (relative) component:

$$\Delta\mathrm{NEE} = \epsilon_{\mathrm{abs}} + \epsilon_{\mathrm{rel}} \cdot \mathrm{NEE}, \tag{13}$$

with Gaussian parametrization

$$\epsilon_{\mathrm{abs}} \sim \mathcal{N}(0, \sigma^2_{\mathrm{abs}}), \qquad \epsilon_{\mathrm{rel}} \sim \mathcal{N}(0, \sigma^2_{\mathrm{rel}}). \tag{14}$$

Across all scenarios, we set $\sigma_{\mathrm{abs}} = 1.5\,\mu\mathrm{mol\,CO_2\,m^{-2}\,s^{-1}}$ and $\sigma_{\mathrm{rel}} = 8\%$.

4.2 Flux partitioning

The simulated datasets are fitted using the neural network architecture described in Sect. 3. Figure 8 shows the resulting model performance for NEE, GPP, and R_{eco} for a representative case with $\kappa = 0.3\,\mathrm{kPa}^{-1}$ and added random noise.

Under these controlled conditions, the neural network reproduces the simulated carbon fluxes with high accuracy across all components. The coefficient of determination R^2 is very close to 1 in all cases, meaning nearly perfect description of the data by the model. By construction, noise was added only to net ecosystem exchange (NEE), while GPP and R_{eco} remain noise-free, which explains the comparatively lower R^2 values for NEE. The strong predictive performance for GPP and R_{eco} indicates that the model successfully recovers the underlying functional relationships despite the presence of noise in NEE.

We conclude that, under the assumptions of a simplified flux model, the neural-network approach is capable of accurately representing NEE and effectively disentangling GPP and R_{eco}.

4.3 Extracting temperature dependencies

In a second step, we use the simulated datasets to analyze the functional dependencies learned by the model. A key advantage of the neural-network approach, compared to traditional daytime (DT)/nighttime (NT) partitioning schemes, is its ability to learn relationships between meteorological and satellite-based drivers and the latent flux components directly from the data. Conceptually, the model represents a nonlinear mapping,

$$\mathrm{NEE} = -f_{\mathrm{GPP}}(T, \mathrm{RH}, \mathrm{NIRv}, \ldots) + f_{R_{\mathrm{eco}}}(T, \mathrm{NIRv}, \ldots), \tag{15}$$

where f_{GPP} and $f_{R_{\mathrm{eco}}}$ denote the subnetworks predicting gross primary productivity and ecosystem respiration, respectively.

To interpret the learned relationships, we analyze individual conditional expectation (ICE) curves and partial dependence plots (PDPs) for GPP and R_{eco}. ICE curves describe the response of the model output to a given variable for individual samples,

https://doi.org/10.5194/egusphere-2026-4847
Preprint. Discussion started: 24 August 2026

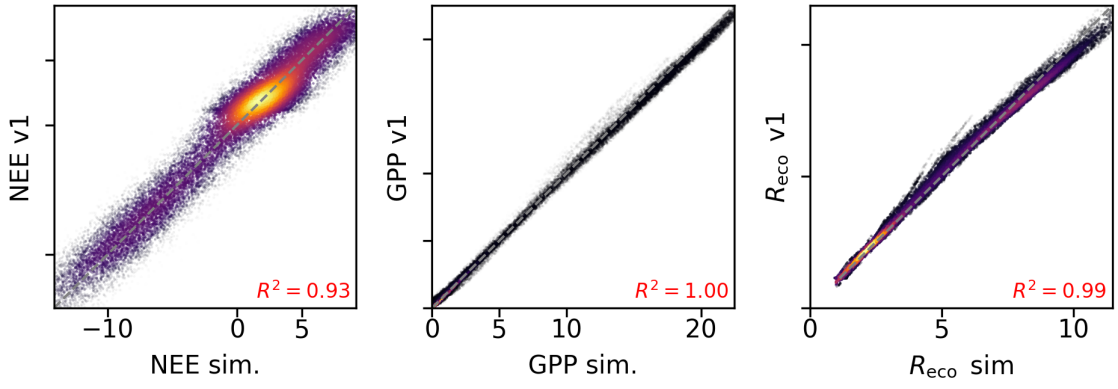

Figure 8. Scatter plots comparing the `pyVPRNN_v1` partitioning for $\kappa = 0.3\,\mathrm{kPa}^{-1}$ and EVI-scaling as described in Sect. 4. The left panel shows the comparison to the total NEE (including noise), the middle panel shows the comparison to GPP (without noise) and the right panel shows the comparison to R_{eco} (without noise). Colors indicate point density. Abbreviations are as follows: sim. = simulation, v1 = `pyVPRNN_v1`. All fluxes are given in units of $\mu\mathrm{mol\,CO_2\,m^{-2}\,s^{-1}}$. The x- and y-axes share the same limits and tick intervals in all cases.

thereby revealing heterogeneity in the learned relationships across environmental conditions. PDPs, in contrast, represent the average response over all samples and thus summarize the dominant functional dependency.

Both ICE curves and PDPs reflect the relationships learned by the model given the selected predictor set, data coverage, and neural-network architecture. If the model specification is sufficiently comprehensive – i.e. if the dominant drivers of the target flux are represented – these diagnostics approximate the underlying functional relationships of the system. However, omitted variables or strong correlations among predictors may bias the inferred dependencies, as the model compensates for missing information using the available predictors. Consequently, the interpretation of ICE curves and PDPs depends on an adequate representation of the relevant environmental and physiological controls.

An important choice is the use of relative humidity instead of VPD in our model setup (Fig. 5). Together with temperature, VPD and RH are informationally equivalent. Though VPD is more directly linked to plant physiological responses, it is also strongly correlated with temperature. Relative humidity exhibits substantially weaker co-linearity with temperature, facilitating a more robust interpretation of the learned temperature dependencies.

To evaluate whether the network recovers the temperature relationships correctly, we analyze the learned temperature using ICE curves and PDPs. In fact, under the assumption that temperature effects can be factorized for GPP and R_{eco}, Eq. 15 may be approximated as

$$\mathrm{NEE} = -f_{T,\mathrm{GPP}}(T) \cdot f_{\mathrm{GPP}}(\mathrm{RH}, \mathrm{EVI}, \ldots) + f_{T,R_{\mathrm{eco}}}(T) \cdot f_{R_{\mathrm{eco}}}(\mathrm{EVI}, \ldots), \tag{16}$$

where $f_{T,\mathrm{GPP}}$ and $f_{T,R_{\mathrm{eco}}}$ denote effective temperature-response functions. In this formulation, ICEs and PDPs for temperature align and capture an unambiguous ecosystem response to temperature. Note that the resulting temperature relationships include both direct physiological effects and indirect effects mediated by the vapor-pressure deficit (VPD) term, given that temperature

https://doi.org/10.5194/egusphere-2026-4847
Preprint. Discussion started: 24 August 2026

and relative humidity jointly determine VPD (Medlyn et al., 2011; Leuning, 1995). As a consequence, the apparent temperature optimum of photosynthesis shifts to lower values with increasing sensitivity to VPD (i.e. a higher κ as defined in Sect. 4.1). In principle, replacing relative humidity with VPD as an explicit input could help to disentangle direct temperature effects from stomatal limitations. In practice, however, this separation requires careful treatment due to the strong correlation between temperature and VPD.

In Fig. 9, we compare the learned temperature response to the reference functions for the case of $\kappa = 0.0\,\mathrm{kPa}^{-1}$ with EVI-dependent scaling. In this configuration, the GPP formulation reduces to standard VPRM. For R_{eco}, we consider absolute flux magnitudes, whereas for photosynthesis we analyze the normalized temperature response, GPP/GPP$_{\mathrm{max}}$, in order to isolate the functional shape independent of magnitude (cf. Eq. 11 and Eq. 12).

For the partial dependence analysis of photosynthesis, we restrict the parameter space to conditions of high leaf density (NDRE between the 85th and 95th percentiles) and high solar irradiance (also between the 85th and 95th percentiles). Consequently, variability in NDRE is limited in the GPP analysis, and NDRE is therefore not shown explicitly, in contrast to R_{eco}. The highest values of NDRE and irradiance are excluded to avoid sparse sampling in the high-dimensional parameter space.

In order to evaluate whether our approach is also able to identify combined temperature and VPD effects, we have run our simulation with $\kappa = 0.3\,\mathrm{kPa}^{-1}$ and $\kappa = 1.0\,\mathrm{kPa}^{-1}$ and with and without random noise added. The resulting PDP plots are shown in Figure 10. For comparison also the underlying truth is shown for different relative humidities. It is given by the product of T_{scale} (see eq. 12) and the exponential VPD term rewritten in terms of temperature (in degrees celsius) and relative humidity

$$\mathrm{VPD}_{\mathrm{scale}}(T, \mathrm{RH}) = \exp\left[-\kappa(1 - \mathrm{RH}) \cdot e_s(T)\right], \tag{17}$$

where the saturation vapor pressure ($e_s(T)$ in kPa) can be expanded using Tetens' equation

$$e_s(T) = 0.611 \exp\left(\frac{17.27\,T}{T + 237.3}\right). \tag{18}$$

By construction, this leads to a shift of the temperature optimum toward lower temperatures, which becomes more pronounced with increasing κ and decreasing relative humidity, as higher vapor pressure deficit induces stronger suppression of GPP at elevated temperatures.

Overall, the partial dependence plots (PDPs) recover the underlying response more accurately in the absence of random noise. In the case of $\kappa = 0.3\,\mathrm{kPa}^{-1}$, the small shift in the temperature optimum under low relative humidity conditions is not well captured. This is expected, as the $\mathrm{VPD}_{\mathrm{scale}}$ changes the flux only by approximately 5% for the median site VPD of $0.19\,\mathrm{kPa}$ which is smaller than the random noise. In contrast, for higher values of κ, the stronger shift in the temperature optimum is well reproduced by the model, both with and without added noise.

Our controlled setup is simpler than real eddy covariance observations: there are no disturbances, environmental drivers are nearly fully represented in the model inputs, and functional relationships are simplified. Nevertheless, these results demonstrate that, under sufficiently complete model specifications, our neural-network setup in combination with ICE and PDP diagnostics can recover process-level relationships from flux data and provide novel insight into ecosystem functions.

https://doi.org/10.5194/egusphere-2026-4847
Preprint. Discussion started: 24 August 2026

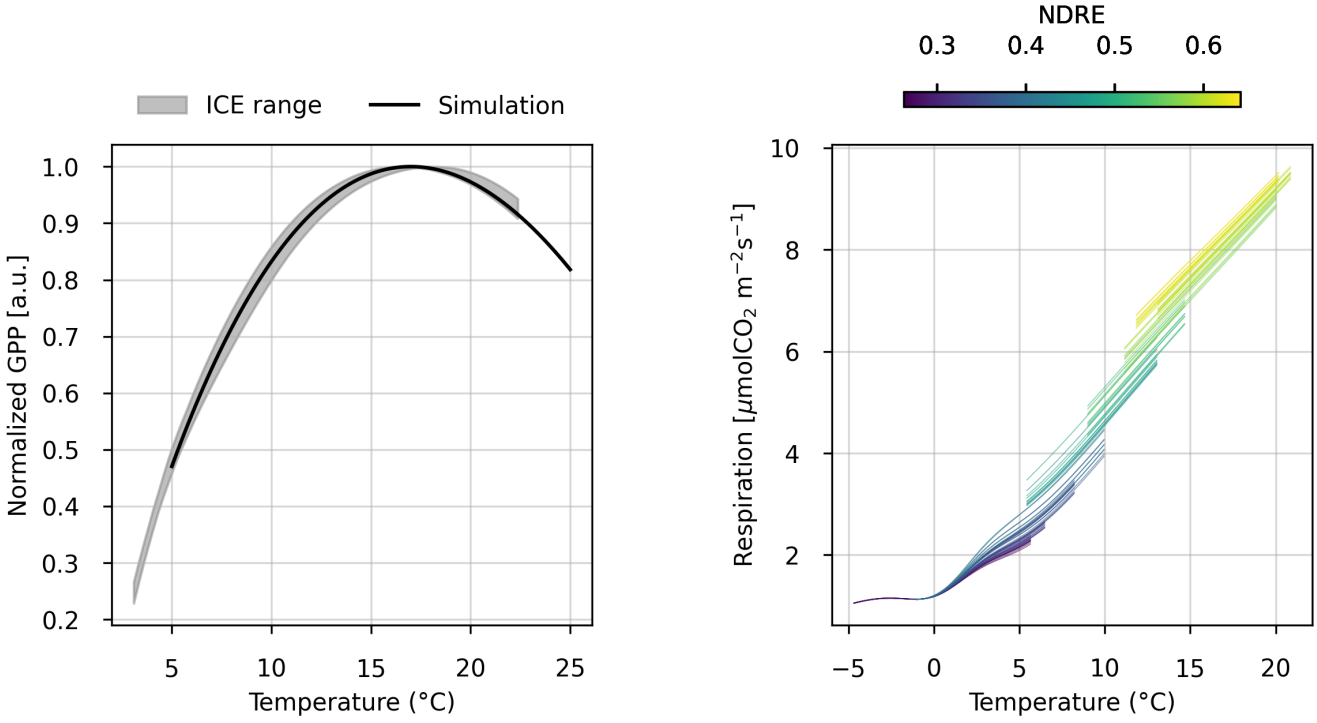

Figure 9. Partial dependence of the `pyVPRNN_v1` model with respect to temperature for simulated flux data with $\kappa = 0.0, \mathrm{kPa}^{-1}$, shown for gross primary productivity (GPP, left) and ecosystem respiration (R_{eco}, right). For GPP, responses are normalized by $\mathrm{GPP}_{\mathrm{max}}$. Individual conditional expectation (ICE) curves for R_{eco} are colored by NDRE, as indicated by the color bar. For GPP, the shaded region indicates the 5th–95th percentile range of the ICE curves. The true simulated temperature dependence is shown as a solid black line. ICE curves are restricted to the observed temperature range to avoid extrapolation artifacts.

5 Results

Following the procedure described in Sect. 3.3, we trained the `pyVPRNN_v1` neural-network model separately for each of the 32 eddy covariance sites listed in Table 2. The trained models were then used to predict GPP and R_{eco} for all times for which a flux footprint could be calculated, however we focus on the actually measured timestamps (NEE_VUT_REF_QC=0) for our three complementary evaluation strategies. First, we compared statistical performance metrics across all partitioning approaches and sites, both against observations and relative to one another. Second, we analyzed the diurnal cycles at the example sites DK-Sor and SE-Svb in order to assess differences in the temporal behavior of the partitioning methods. Third, we investigated the partial dependence of the neural-network-derived fluxes on temperature at these two sites to assess whether the inferred relationships are ecologically plausible and consistent with established process understanding.

We use two complementary metrics to evaluate model performance: the coefficient of determination (R^2), which quantifies the proportion of variance in the observed data explained by the model, and the reduced χ^2, which assesses whether model

https://doi.org/10.5194/egusphere-2026-4847
Preprint. Discussion started: 24 August 2026

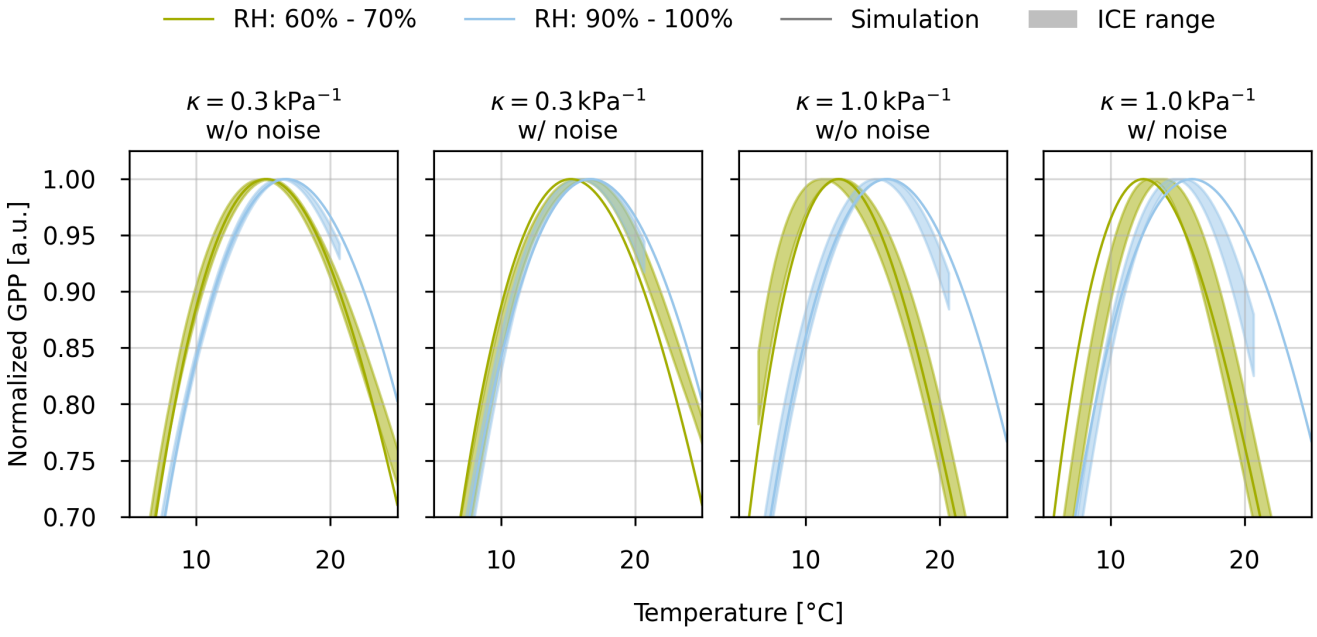

Figure 10. Temperature dependence of GPP for simulations with different values of κ and with or without added random noise (see Sect. 4.1). The prescribed temperature response used to generate the simulations is shown as a solid line, while the corresponding ranges of the individual conditional expectation (ICE) curves are shown as shaded bands. Different colors denote different ranges of relative humidity (RH), as indicated in the legend.

residuals are consistent with the observational uncertainty. Values of R^2 close to 1 indicate strong agreement, whereas values close to 0 indicate limited explanatory power; χ^2 values close to 1 indicate that residuals are, on average, consistent with the stated measurement uncertainty, i.e. the model is consistent with the data. We evaluate these metrics in two complementary ways: first, with respect to observed NEE, separately for daytime and nighttime conditions, reporting both R^2 and χ^2 wherever a comparison is made against observed NEE; and second, by comparing derived flux components (GPP and R_{eco}) directly across partitioning approaches, for which we report R^2 only, since these comparisons do not involve a quantity with a defined measurement uncertainty.

Figure 11 and Figure 12 compare observed NEE against the different partitioning approaches during daytime (top panel) and nighttime (bottom panel) using R^2 and χ^2, respectively. For daytime, we compare DT partitioning and `pyVPRNN_v1`, since both estimate GPP and R_{eco} independently; NT partitioning is not shown because it forces NEE to close by construction. For nighttime, NT partitioning is included by forcing GPP to zero, since the estimated R_{eco} alone can then be compared directly against observed nighttime NEE.

For daytime NEE, R^2 is mostly between 0.6 and 0.9 for both partitioning approaches, with site-by-site variation being larger than the difference among the partitioning algorithms in the majority of cases. χ^2 values range mostly between 1 and 3, with

https://doi.org/10.5194/egusphere-2026-4847
Preprint. Discussion started: 24 August 2026

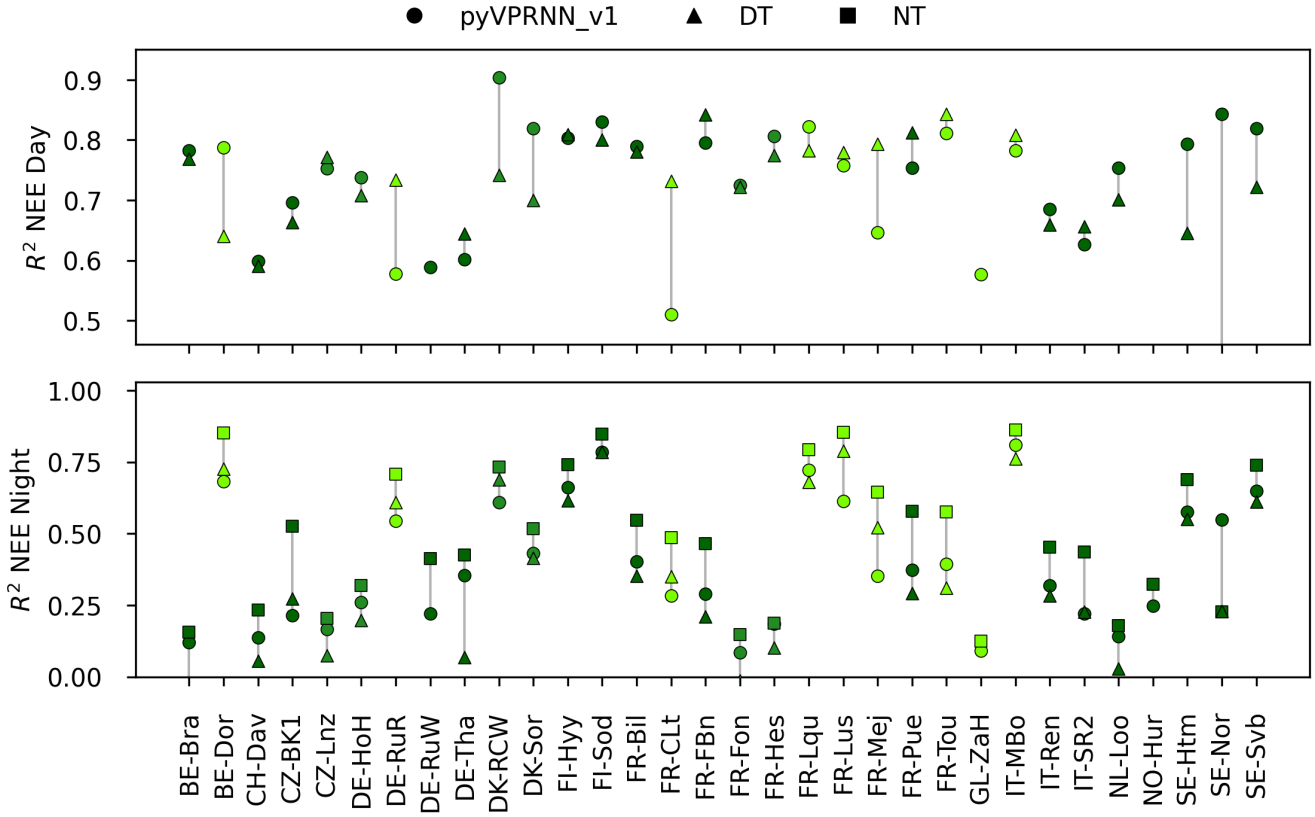

Figure 11. Agreement between partitioned fluxes and observed NEE for daytime (top row) and nighttime (bottom row) conditions across all sites. Different colours indicate vegetation types (light green: grassland, medium green: deciduous forest, dark green: evergreen forest; see also Fig. 13), and different markers denote the partitioning approaches. NT partitioning is not shown in the daytime panels because NEE is not independently reconstructed in this case. For the nighttime comparison, NT-derived GPP is set to zero, such that ecosystem respiration directly corresponds to NEE under nighttime conditions. Note the different y-axis between the panels.

https://doi.org/10.5194/egusphere-2026-4847
Preprint. Discussion started: 24 August 2026

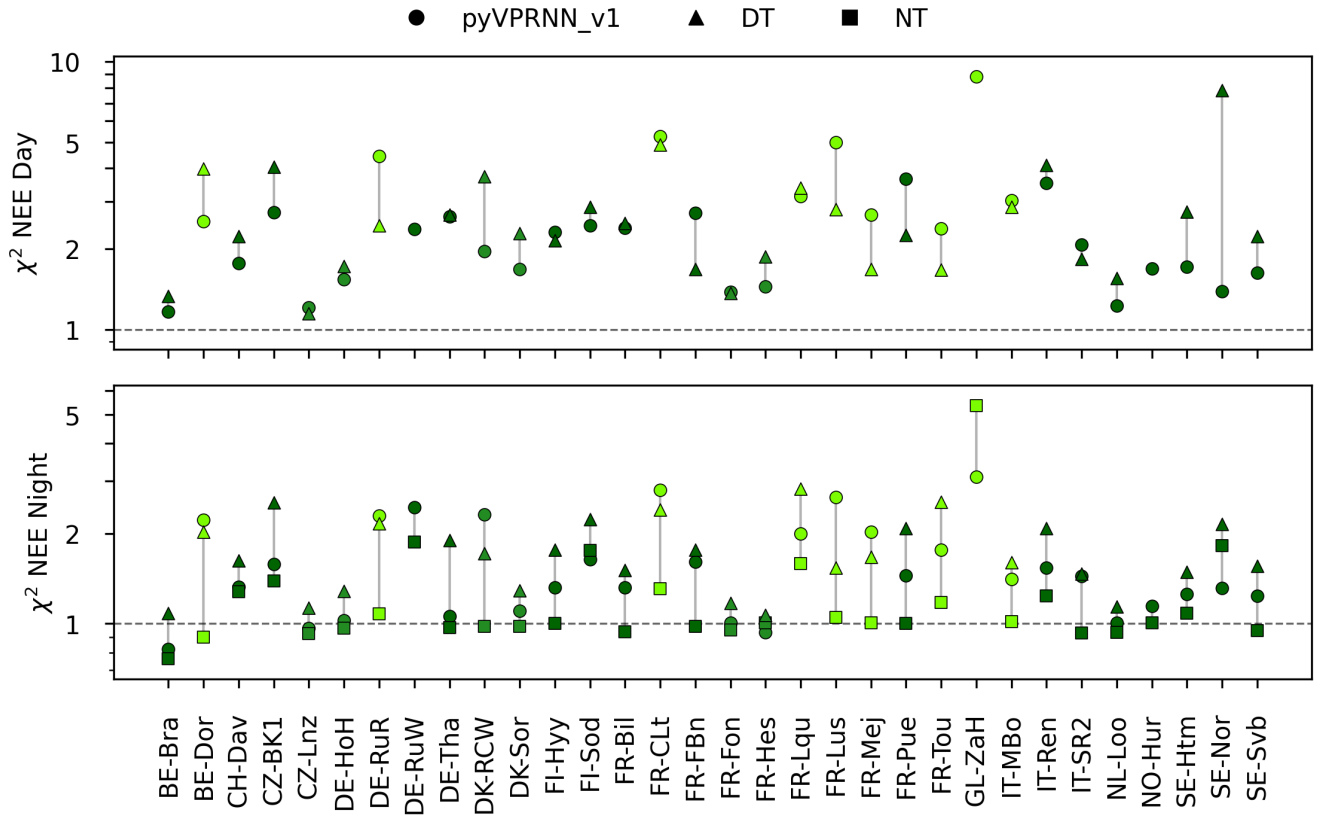

Figure 12. Agreement between partitioned fluxes and observed NEE for daytime (top row) and nighttime (bottom row) conditions across all sites, evaluated using the reduced χ^2. The dashed horizontal line marks $\chi^2 = 1$, indicating residuals consistent with the stated observational uncertainty (NEE_VUT_REF_JOINTUNC); values above this line indicate residuals larger than expected from measurement uncertainty alone. See Figure 11 for more information. Note the different y-axis between the panels.

some outliers to larger values. There are some notable sites: for example, `pyVPRNN_v1` particularly stands out for daytime NEE at DK-RCW ($R^2 = 0.90$), DK-Sor ($R^2 = 0.82$), and BE-Dor ($R^2 = 0.79$), while at the grassland sites FR-Mej, FR-CLt, and DE-RuR, DT R^2 is significantly higher, with `pyVPRNN_v1` reaching only $R^2 = 0.65$, 0.51, and 0.58, respectively. In most cases, higher R^2 also corresponds to χ^2 values closer to one; there are, however, exceptions – at FR-CLt, for instance, R^2 is much higher for DT partitioning, yet χ^2 does not clearly favor either model. At the polar site GL-ZaH, DT partitioning is not available at all, highlighting limitations of conventional approaches under extreme conditions. More generally, DT partitioning produces higher daytime R^2 values than `pyVPRNN_v1` for all grassland sites with frequent cutting events (DE-RuR, FR-Lus, FR-Mej, FR-Tou, IT-MBo), whereas `pyVPRNN_v1`'s R^2 is higher and χ^2 closer to one at the large majority of forest sites.

For nighttime NEE, NT partitioning achieves the highest R^2 values across all sites (except SE-Nor). But all three partitioning approaches exhibit strong variation ranging from values close to zero (e.g. FR-Fon, NL-Loo) to above 0.8 (e.g. BE-Dor, FI-

https://doi.org/10.5194/egusphere-2026-4847
Preprint. Discussion started: 24 August 2026

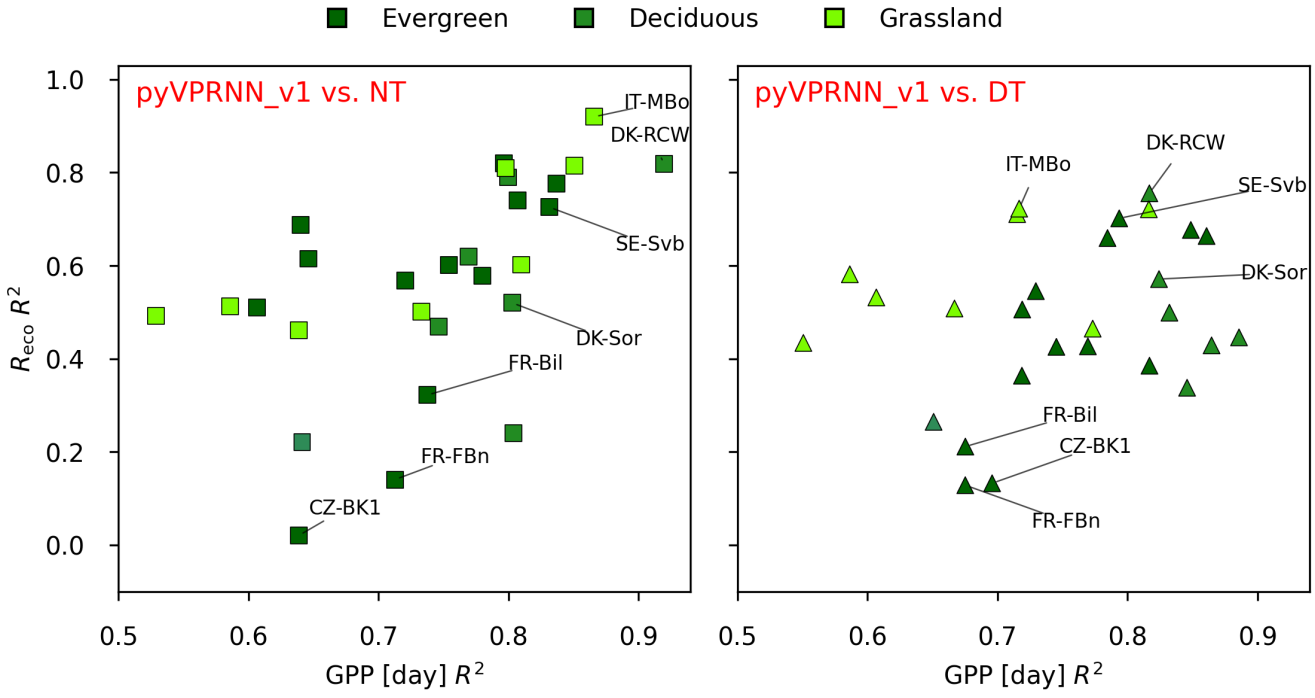

Figure 13. Two-dimensional scatter plots showing agreement (expressed as R^2) in GPP (horizontal axis) and R_{eco} (vertical axis) between `pyVPRNN_v1` versus NT partitioning (left panel) and versus DT partitioning (right panel). Colours indicate vegetation classes as shown in the legend. Marker styles correspond to those used in Fig. 11. The axes are clipped to enhance readability; a small number of extreme outliers fall outside the displayed range. Sites with the largest deviations are labelled explicitly. Complete site-level values are provided in Tables A2 and A3.

Sod). Grassland sites generally have lower outlier to small R^2 values than forest types. Notably, χ^2 values cluster closer to 1 than for daytime data; low R^2 values are thus in many cases still associated with χ^2 close to 1 – for example, the evergreen forest site BE-Bra has a nighttime R^2 of 0.12 for `pyVPRNN_v1` but a χ^2 of 0.82. At CZ-BK1 NT partitioning has an R^2 of 0.52, while `pyVPRNN_v1` has only 0.21. Nevertheless the χ^2 is quite similar making neither model strongly favored. Overall, a high daytime R^2 for `pyVPRNN_v1` or DT partitioning does not necessarily imply a high nighttime R^2.

In Figure 13, we compare the similarity of GPP and R_{eco} estimates between partitioning approaches, specifically `pyVPRNN_v1` versus NT partitioning (left panel) and `pyVPRNN_v1` versus DT partitioning (right panel), across all sites. Overall, GPP estimates show higher agreement between approaches than R_{eco}, with R^2 values mostly above 0.6, whereas R_{eco} exhibits lower consistency, with R^2 ranging essentially between zero and one. `pyVPRNN_v1` and DT agree more consistently for GPP, while NT shows a larger number of lower-R^2 outliers. Across sites, `pyVPRNN_v1` versus NT shows a weak positive correlation, such that higher GPP agreement tends to be accompanied by higher R_{eco} agreement; the DT comparison shows no such structure, with several cases of high GPP agreement paired with low R_{eco} agreement.

https://doi.org/10.5194/egusphere-2026-4847
Preprint. Discussion started: 24 August 2026

Some notable site-level patterns emerge. For example, the deciduous forest site DK-RCW shows similarly high agreement for both partitioning approaches. In contrast, the evergreen forest sites CZ-BK1 and FR-FBn show markedly lower agreement, particularly for R_{eco} ($R^2 < 0.2$). More generally, grassland sites do not exhibit the very-low-R^2 outliers seen among some forest sites.

In addition to the summary statistics, diurnal cycles provide further insight into the differences between the approaches. Figures 14 and 15 show the mean monthly diurnal cycles for DK-Sor and SE-Svb, respectively. Overall, observed NEE and the partitioning approaches agree well, both across seasons and between years. Notable deviations do occur among the partitioned fluxes, however – most visibly in summer-month respiration. For SE-Svb R_{eco} in the summer month is rising higher during daytime than for the other approaches. In contrast, for DK-Sor R_{eco} is reducing during daytime (with rising temperature) in contrast to the other partitioning algorithms as also shown in Figure 18. In both cases GPP are also shifted in a way that overall NEE dynamics are still well captured.

Finally, the partial dependence (PDP) and individual conditional expectation (ICE) analyses reveal distinct temperature responses of both GPP and R_{eco}. Results for SE-Svb and DK-Sor are shown in Figs. 16 and 18, respectively. For GPP, both sites exhibit low carbon uptake at low temperatures, followed by increasing uptake with temperature, peaking at intermediate temperatures before declining at higher temperatures. While the peak occurs around 13°C at DK-Sor, it is around 18°C at SE-Svb. The ICE curves show relatively limited spread across the temperature range, indicating that the inferred temperature response is largely robust with respect to other model inputs within the explored domain.

The inferred temperature dependence of R_{eco} also varies between the two sites. Respiration is consistently low at low temperatures and increases with warming, but the functional form differs, ranging from approximately linear to strongly nonlinear responses. At the evergreen forest site SE-Svb, ecosystem respiration increases monotonically with temperature, with little dependence on vegetation index variability. At the deciduous forest site DK-Sor, the response is more complex, with respiration increasing with both temperature and NDRE, and declining at temperatures above approximately 13°C.

Overall, the PDP and ICE analyses demonstrate that the neural networks learn coherent and site-specific temperature dependencies for both GPP and R_{eco}, consistent with established ecological process understanding.

6 Discussion

GPP and R_{eco} are not directly observable, and biases in the two flux components may compensate each other, so evaluating partitioning performance remains inherently challenging as the underlying truth remains unknown. Flux partitioning is therefore fundamentally underconstrained without additional information on ecosystem processes. Different partitioning schemes may reproduce NEE equally well while yielding notably different estimates of GPP and R_{eco}, as Sect. 5 has shown. Even where predictive performance for NEE is similar, the approaches differ fundamentally in their underlying assumptions and domains of applicability. These structural differences become particularly important for complex ecosystem functions, under heterogeneous environmental conditions, during periods of ecosystem disturbance, or when models are applied beyond the conditions under which they were calibrated.

https://doi.org/10.5194/egusphere-2026-4847
Preprint. Discussion started: 24 August 2026

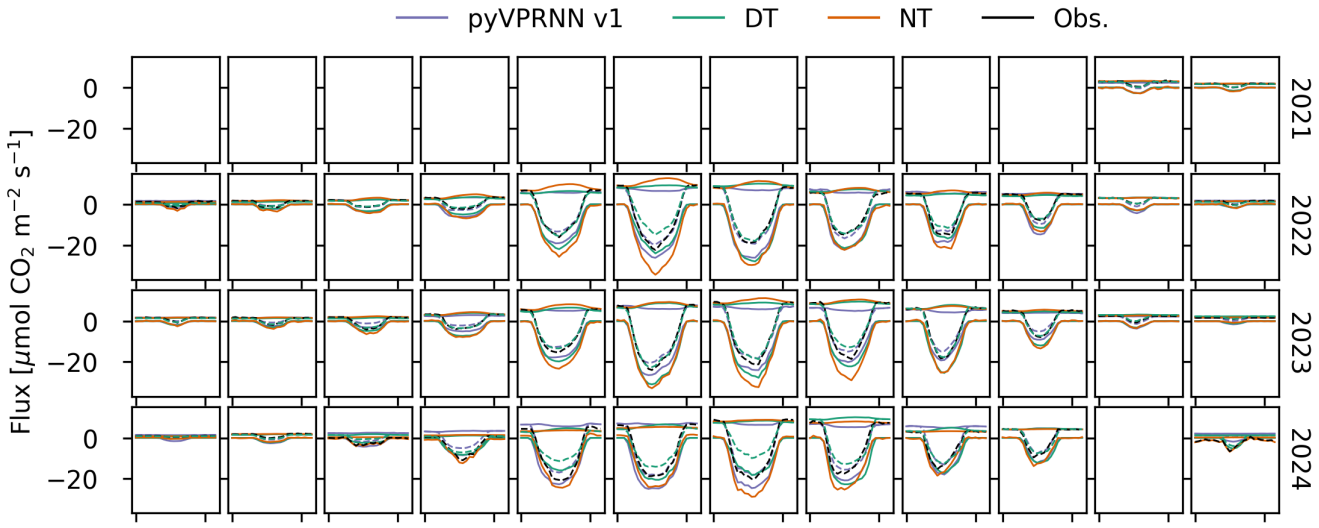

Figure 14. Monthly mean diurnal cycles for the deciduous broadleaf forest site DK-Sor. Each panel shows the average diurnal cycle for a given month, with panels arranged from January (left) to December (right). Rows correspond to individual years (indicated on the right). Diurnal cycles are shown separately for ecosystem respiration (R_{eco}, positive solid lines), gross primary productivity (GPP, negative solid lines), and net ecosystem exchange (NEE, dashed lines). Colors distinguish different partitioning approaches: NT (nighttime), DT (daytime), `pyVPRNN_v1` (neural-network model), and Obs. (tower observations). Note that for NT-partitioning no NEE line is shown since it is by definition equal to the observations.

The `pyVPRNN_v1` model presented in this paper follows a fundamentally different approach than the traditional DT- and NT-based methods. It provides a single, consistent data-driven biosphere model for the entire data period, aiming to represent variations in GPP and R_{eco} through continuous variation of the driver variables and their spatiotemporal evolution. The traditional approaches, in contrast, provide a sequence of models with fixed mathematical form, re-optimized in moving time windows of a few weeks.

Nighttime respiration is best represented by the NT partitioning approach, in terms of both R^2 and χ^2. This is by construction, as NT partitioning is explicitly calibrated to reproduce (the sparse) nighttime observations, with repeated fits over time windows of a few weeks. This advantage, however, comes with important limitations. During nighttime, atmospheric conditions are often stable and turbulence is weak, which increases uncertainty in eddy-covariance measurements, limits data availability, and generally extends the flux footprint farther upwind (Figure 1), producing biases when the nighttime model is extrapolated to daytime conditions. This is evidenced by a non-negligible fraction of unphysical (negative) GPP values during daytime, with a median of 10% of daytime GPP values being negative across all 32 sites. Data sparsity is a particular problem for nighttime observations: Figure 17 shows a few weeks of half-hourly observations at DK-Sor in July 2023 (where turbulence is comparably high), where many consecutive days lack any nighttime NEE measurement at all, limiting the accuracy of the nighttime fit. Furthermore, meteorological conditions differ substantially between night and day, and the simple analytical as-

https://doi.org/10.5194/egusphere-2026-4847
Preprint. Discussion started: 24 August 2026

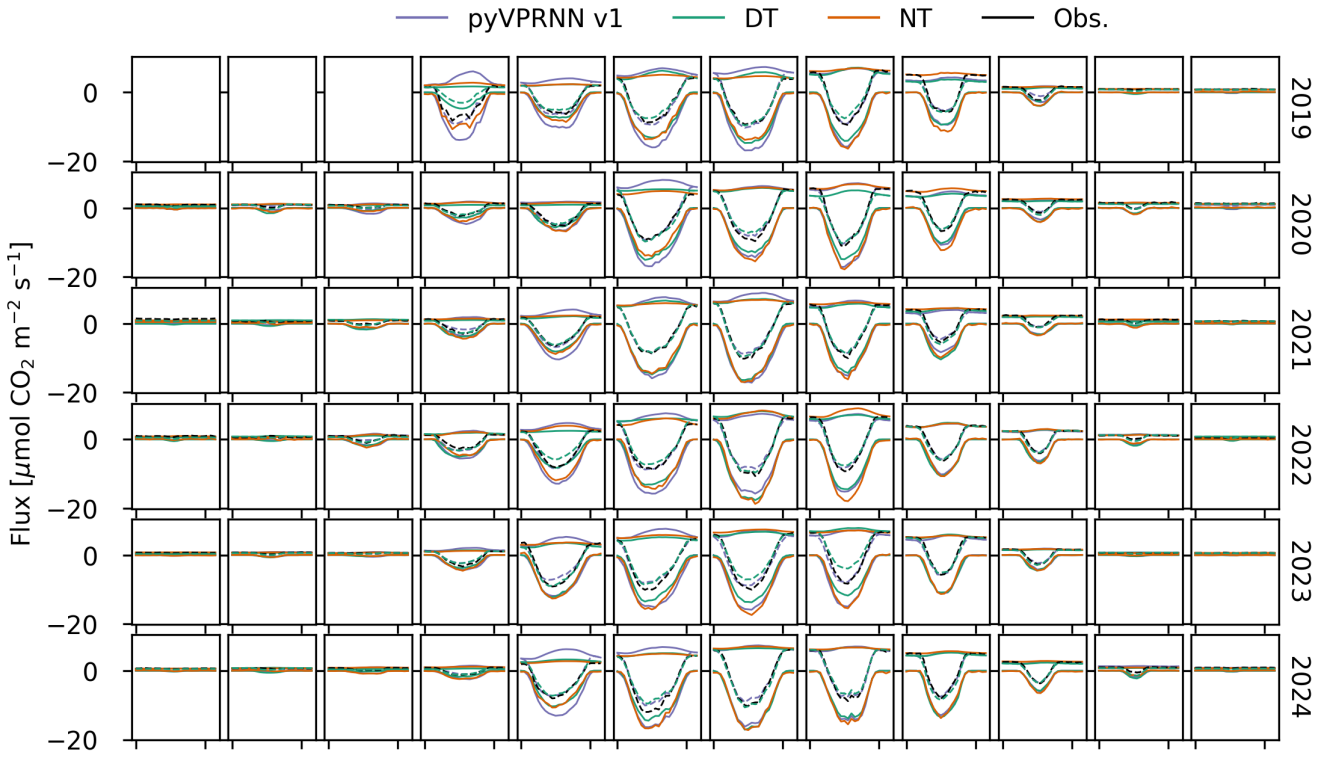

Figure 15. Monthly mean diurnal cycles for the deciduous broadleaf forest site SE-Svb. Each panel shows the average diurnal cycle for a given month, with panels arranged from January (left) to December (right). Rows correspond to individual years (indicated on the right). Diurnal cycles are shown separately for ecosystem respiration (R_{eco}, positive solid lines), gross primary productivity (GPP, negative solid lines), and net ecosystem exchange (NEE, dashed lines). Colors distinguish different partitioning approaches: NT (night-time), DT (day-time), `pyVPRNN_v1` (neural-network model), and Obs. (tower observations).

sumption of a Q10-type respiration function may not hold under daytime conditions. DK-Sor, for example, shows a unimodal temperature response that declines above a certain optimal temperature (Figure 18) – a pattern documented in the literature (Niu et al., 2024a), but one that can barely be constrained by low-temperature nighttime conditions alone. As a consequence, NT partitioning predicts R_{eco} to increase during summer daytime with increasing temperature, while `pyVPRNN_v1` predicts the opposite. By construction, NT partitioning derives daytime GPP as the difference between NEE and R_{eco}; GPP is therefore not a smooth, independent function (as it is for DT partitioning or `pyVPRNN_v1`), but instead directly inherits the measurement noise of NEE, as clearly visible in Figure 17.

In contrast to NT partitioning, DT partitioning provides independent estimates of GPP and R_{eco} and is in this sense more similar to `pyVPRNN_v1`, allowing an independent comparison of daytime and nighttime NEE. Like NT partitioning, however, it re-optimizes its fit in a moving time window of a few weeks, albeit using a more complex rectangular-hyperbolic response

https://doi.org/10.5194/egusphere-2026-4847
Preprint. Discussion started: 24 August 2026

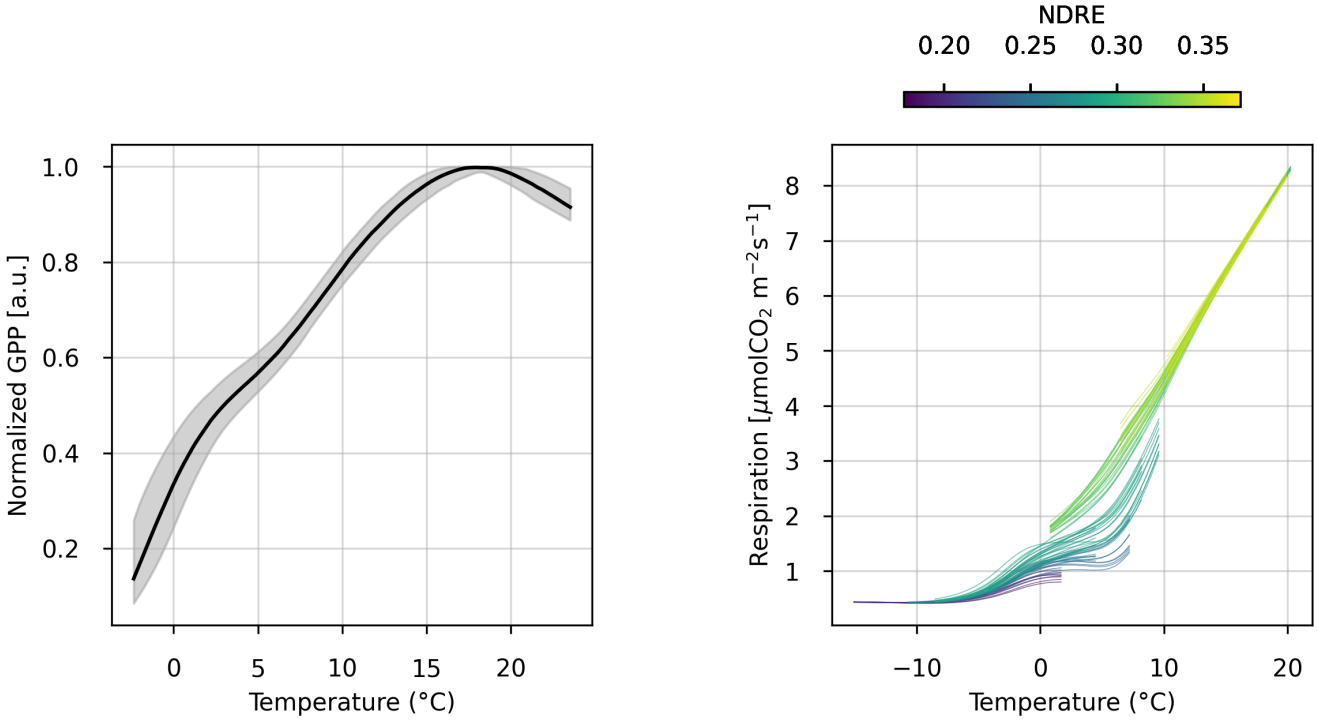

Figure 16. Partial dependence of the `pyVPRNN_v1` model with respect to temperature at the ICOS site SE-Svb for gross primary productivity (GPP, left) and R_{eco} (right). For GPP, the response is normalized by GPP_{max}. Individual Conditional Expectation (ICE) curves for R_{eco} are colored by NDRE, as indicated by the color bars. For GPP, the shaded region indicates the 5th–95th percentile range of the ICE curves. The black solid line shows the corresponding partial dependence. ICE curves are only shown within the range of temperatures represented well sampled in the dataset to avoid extrapolation artifacts.

curve. Depending on the situation, this re-fitting can be either an advantage or a disadvantage. Figure 17 illustrates, using DK-Sor, how sequential fits can produce inconsistent model behavior – visible here before and after July 13 – an inconsistency that can be amplified by unstable conditions with few reliable data points and a footprint expanding across different ecosystems, producing a convoluted signal. Conversely, the moving time window allows both DT and NT partitioning to adapt quickly to disturbances. DT partitioning indeed shows better daytime R^2 than `pyVPRNN_v1` at grassland sites subject to frequent mowing; by construction, it is difficult for `pyVPRNN_v1` to capture such abrupt events from Sentinel-2 imagery alone, since cloud-free temporal resolution is limited to days or weeks (see also the example of IT-MBo in Figure A3). For more stable grasslands – natural grasslands such as FR-Lqu and GL-ZaH, or slowly varying, extensively grazed sites such as BE-Dor – `pyVPRNN_v1` outperforms DT partitioning. FR-CLt is a notable exception, as it is a natural site but snow-covered for more than half of the year, a condition not currently accounted for in our model. `pyVPRNN_v1` similarly performs better at forest sites, which tend to be more temporally stable than human-managed ecosystems; forests are, in addition, generally more com-

https://doi.org/10.5194/egusphere-2026-4847
Preprint. Discussion started: 24 August 2026

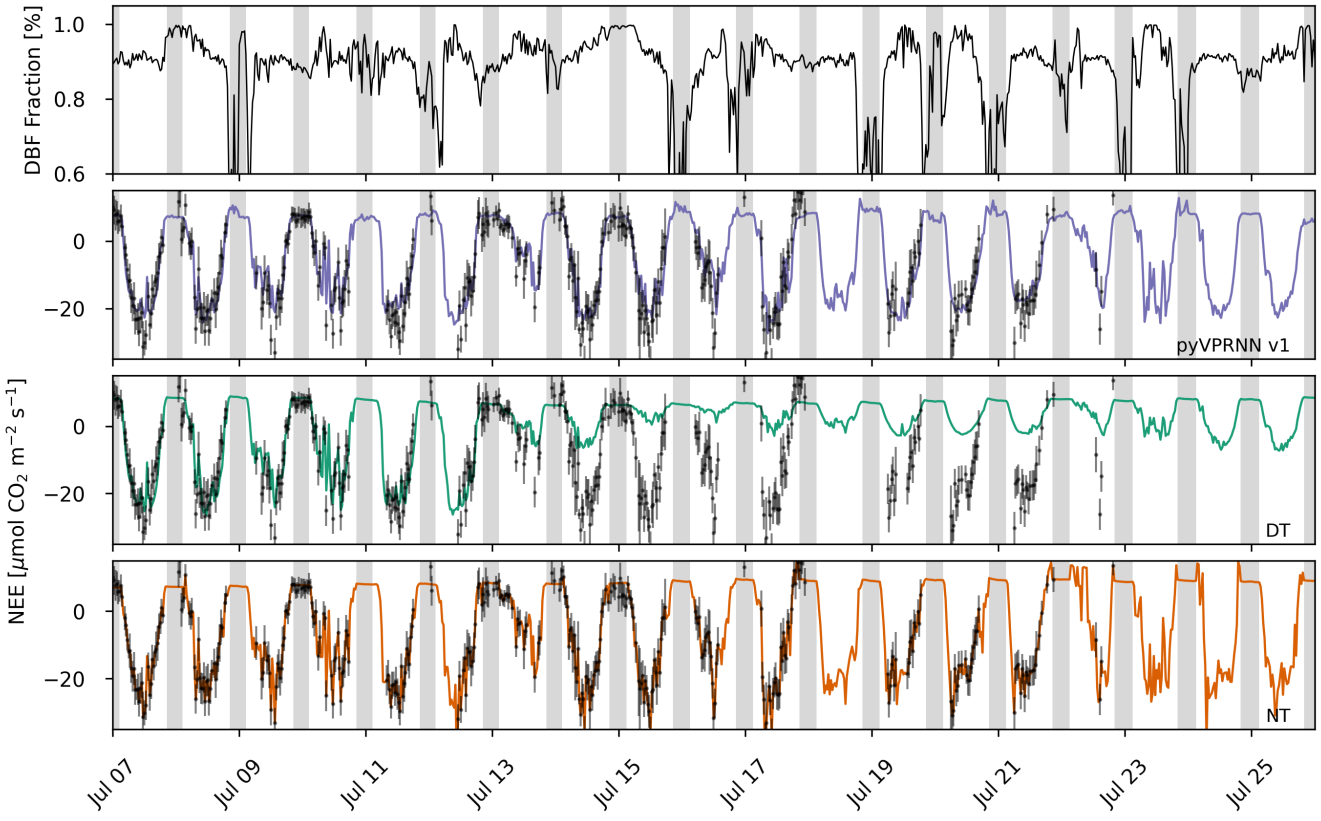

Figure 17. Half-hourly time series at DK-Sor between 7 and 26 July 2023. The top panel shows the fraction of deciduous forest within the tower footprint. The three panels below show NEE as estimated by `pyVPRNN_v1`, DT partitioning, and NT partitioning, respectively. Measured data (NEE_VUT_REF_QC = 0) are shown with 1σ error bars. Shaded areas indicate nighttime. Note that for NT partitioning, the nighttime flux shown is R_{eco} with GPP set to zero by construction.

plex in their carbon–meteorology interactions and dynamics (Jiang et al., 2026), and therefore benefit from `pyVPRNN_v1`'s richer meterological input.

Notably, all partitioning approaches better reproduce nighttime variability (R^2) at grassland sites than at forest sites. This can be understood by the fact that forest canopies are more susceptible to nocturnal CO_2 storage and subsequent flushing (Aubinet et al., 2005), whereas grassland canopies are largely free of this issue, yielding comparatively cleaner nighttime respiration signals. This does not, however, necessarily imply better data–model agreement relative to the stated measurement uncertainty (NEE_VUT_REF_JOINTUNC): nighttime χ^2 shows no clear preference for either vegetation type. In other words, while forest and grassland sites show similar data–model agreement across approaches once measurement uncertainty is accounted for, nighttime observations alone only weakly constrain the models themselves. Consequently, the model intercomparison (Figure 12) shows substantial variability in R_{eco}, i.e. the different approaches predict fundamentally different R_{eco} dynamics.

https://doi.org/10.5194/egusphere-2026-4847
Preprint. Discussion started: 24 August 2026

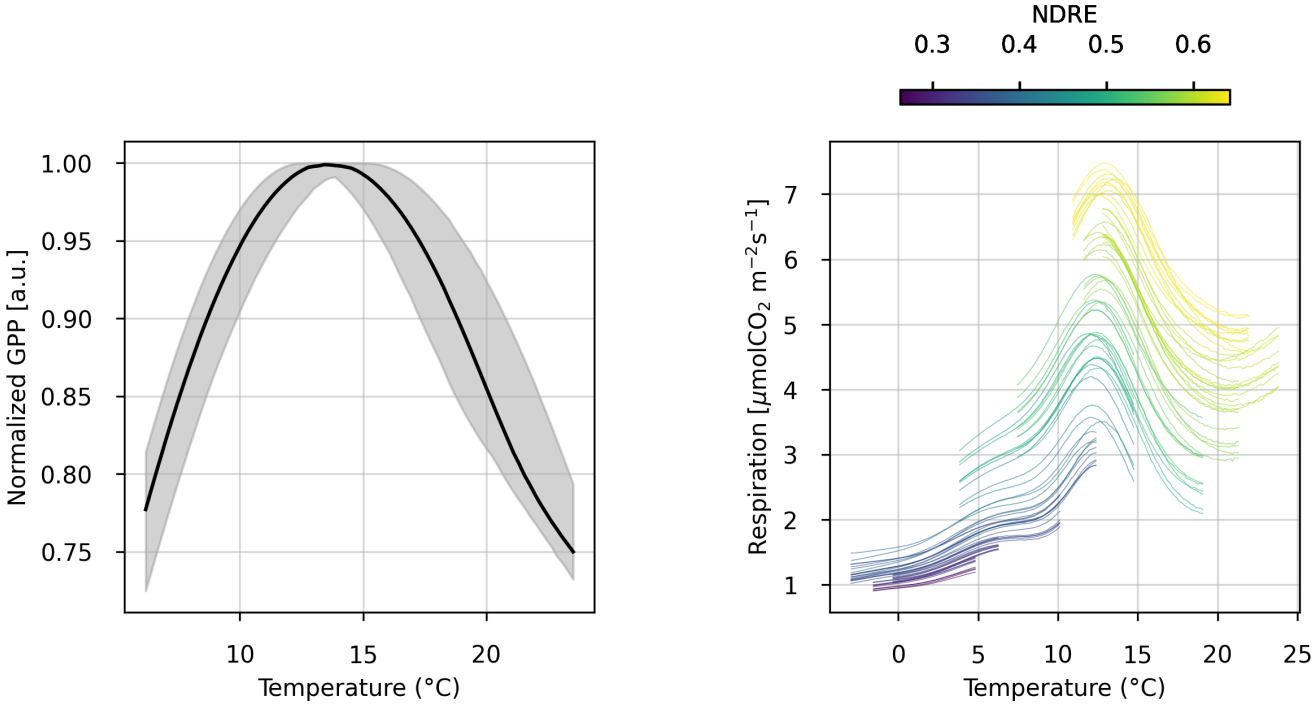

Figure 18. Partial dependence of the `pyVPRNN_v1` model with respect to temperature at the ICOS site DK-Sor for gross primary productivity (GPP, left) and R_{eco} (right). For GPP, the response is normalized by $\mathrm{GPP}_{\mathrm{max}}$. Individual Conditional Expectation (ICE) curves for R_{eco} are colored by NDRE, as indicated by the color bars. For GPP, the shaded region indicates the 5th–95th percentile range of the ICE curves. The black solid line shows the corresponding partial dependence. ICE curves are only shown within the range of temperatures represented well sampled in the dataset to avoid extrapolation artifacts.

This dependence on poorly constrained nighttime respiration is a general disadvantage of NT partitioning relative to the other two approaches, which are more strongly constrained by daytime data.

Overall, these findings point to a conceptual trade-off between `pyVPRNN_v1` and the traditional approaches. Classical partitioning methods achieve strong short-term adaptivity through continuous refitting over relatively short time windows, but rely on simplified, predefined process formulations and do not guarantee long-term consistency. The neural-network approach, in contrast, allows for more flexible, temporally consistent, and generalizable functional relationships, but currently assumes longer-term stationarity in ecosystem functioning. Disturbances, management interventions, and long-term ecosystem change can therefore violate this assumption and degrade model performance if the relevant drivers are not included. This is also why croplands, with their frequent crop rotations, are not included in this study. Two strategies could address time-dependent change: including additional time-dependent information (e.g., time-dependent crop-type maps, or training separate model versions after disturbances) and making use of more frequent satellite observations from hybrid products such as harmonized Sentinel-2/Landsat data (Ju et al., 2025). More generally, splitting the observation window into smaller segments (e.g., year by

https://doi.org/10.5194/egusphere-2026-4847
Preprint. Discussion started: 24 August 2026

year) could help capture slower changes – in soil carbon pools, vegetation composition, or long-term CO_2-fertilization effects associated with rising atmospheric CO_2 (Ainsworth and Long, 2005).

A further conceptual novelty of `pyVPRNN_v1` is its integration of spatiotemporally resolved vegetation indices and land-cover maps to account for spatial heterogeneity around the flux tower. This design naturally resolves biases arising from systematic footprint differences between day and night, morning and afternoon, or across quality flags (Figure 1), helping to separate the ecosystem signal from background noise during model optimization. This explicit spatiotemporal design also helps recover a consistent ecosystem signal during inference – something that has historically been treated as equivalent to the raw measurement. The measurement itself is influenced not only by changes in the underlying vegetation signal but also by footprint variation; the ecosystem signal, by contrast, corresponds to a hypothetical time-independent footprint – which is typically the quantity of actual interest. Much of the nighttime variability shown for `pyVPRNN_v1` in Figure 17 is, in fact, attributable to our choice to display the footprint-dependent expected measurement for consistency. Our approach allows a direct comparison between the inferred signal under the true, time-varying footprint and under a fixed $100\,\mathrm{m} \times 100\,\mathrm{m}$ footprint centered on the tower, which we consider representative of the ecosystem in question. For each site, we compute the average half-hourly relative deviation between GPP and R_{eco} estimated under the true, time-varying footprint versus a fixed $100\,\mathrm{m} \times 100\,\mathrm{m}$ footprint centered on the tower; across all sites tested here, the median of these site-level deviations is around 7% for GPP and 5% for R_{eco} (Figure A4 shows the full distribution) – a subdominant, but at larger scales relevant, difference.

The inferred temperature-response curves (Figs. 16 and 18) are consistent with established physiological and ecological understanding, lending further support to the proposed framework. The GPP curves follow the expected pattern of suppressed carbon uptake at low temperatures and increasing uptake with rising enzymatic activity up to an optimum, beyond which GPP declines. Such unimodal responses are associated with indirect effects of increasing temperature via elevated vapor pressure deficit (VPD), reduced stomatal conductance, and consequently lower photosynthetic uptake (Farquhar et al., 1980; Medlyn et al., 2017). The limited spread of the ICE curves further suggests that temperature exerts a comparatively direct control on GPP at these sites, consistent with the factorized representation of temperature effects proposed in Eq. 16. The inferred temperature optima are, moreover, compatible with typical daytime temperatures during the warmest quarter (Karger et al., 2017), lending additional plausibility to the learned relationships. The respiration responses are likewise consistent with current process understanding (Mahecha et al., 2010; Niu et al., 2024b): the approximately exponential increase observed at the evergreen forest site SE-Svb resembles a classical Q10-type temperature dependence (Lloyd and Taylor, 1994), whereas at the deciduous forest site DK-Sor, the dependence on NDRE indicates a strong seasonal-cycle contribution, with varying relative contributions from heterotrophic and autotrophic respiration – an effect often missed by data-driven models such as VPRM (Glauch et al., 2025; Mahadevan et al., 2008). In particular, the increase of respiration with NDRE is consistent with increasing autotrophic respiration under higher vegetation density.

The overall predictive performance of `pyVPRNN_v1`, together with its ability to recover ecologically plausible temperature-response functions from heterogeneous observational data, suggests that the proposed framework offers more than an alternative partitioning algorithm. In addition to estimating GPP and R_{eco}, it provides a means of extracting process-level information directly from eddy-covariance observations (Sect. 4). We therefore view neural-network-based partitioning not only as a flexi-

https://doi.org/10.5194/egusphere-2026-4847
Preprint. Discussion started: 24 August 2026

ble, data-driven alternative to traditional approaches, but also as a complementary tool for investigating ecosystem responses to environmental drivers. Since `pyVPRNN_v1`'s inputs consist solely of satellite observations, land-cover information, and meteorology, it can also be applied for flux upscaling to similar ecosystems beyond the reach of the flux tower footprint. Because the network is trained on spatially explicit satellite imagery across the full footprint domain, rather than on a single coarse-resolution pixel value per site, it is exposed to intra-footprint spatial heterogeneity that conventional tower-to-global upscaling approaches (Jung et al., 2020) do not capture. This is not only a more accurate treatment it is also a strong regularization to the network training increasing stability.

7 Conclusion and Outlook

In this study, we presented a process-aware neural-network-based biosphere model for partitioning net ecosystem exchange into gross primary production and ecosystem respiration using Sentinel-2 satellite observations, land-cover information, tower footprints, and meteorological data. The model was applied to 32 eddy covariance sites from the ICOS database (RI et al., 2025). These include all forest and grassland sites for which the available meteorological data enabled reliable footprint calculations. Cropland sites were excluded because they do not have a single time-independent ecosystem function and therefore require dedicated treatment, for example by incorporating site-specific crop calendars.

Because GPP and R_{eco} are latent variables, direct quantitative comparisons between partitioning approaches are only possible under limited conditions. We evaluated the different methods against nighttime NEE, used as a proxy for nighttime ecosystem respiration, and additionally compared the daytime (DT) partitioning approach and the neural network against total observed NEE. Overall, `pyVPRNN_v1` outperforms daytime partitioning for stationary ecosystems, i.e. without major and abrupt disturbances or management, and avoids typical biases and uncertainties that arise from NT partitioning. Importantly, `pyVPRNN_v1` relaxes several assumptions inherent to conventional approaches: it can accommodate heterogeneous landscapes and temporally varying flux footprints, does not rely on predefined functional parameterizations, and exploits the full dataset simultaneously to derive a single, consistent model of the ecosystem surrounding the tower.

To assess whether the network learned ecologically meaningful relationships, we performed a partial dependence analysis of the temperature response of GPP and R_{eco}. The inferred relationships are consistent with established ecological theory. In addition, a simulation experiment – with simplified assumptions – demonstrated that the proposed framework can recover the underlying temperature response functions directly from the neural-network model.

The current implementation is particularly well suited to stationary ecosystems such as forests and natural grasslands, and to conditions where the simplified process assumptions of traditional approaches break down, such as in polar or tropical regions. It can be run for individual sites using the implementation in `pyVPRM` [3] (Glauch et al., 2025), and we propose it as a complement to the standard processing in large networks such as ICOS, AmeriFlux, or FLUXNET.

[3] https://github.com/tglauch/pyVPRM

https://doi.org/10.5194/egusphere-2026-4847
Preprint. Discussion started: 24 August 2026

In principle, the method also enables the separation of flux contributions from different land-cover classes within the tower footprint, thereby disentangling ecosystem-specific fluxes at a single site. This aspect will be explored in more detail in future studies and compared with complementary approaches such as flux inversion frameworks like FLUGS (Schlutow et al., 2026).

In ecosystems with strong management, disturbance effects, or pronounced temporal changes in vegetation composition, such as croplands, the model would need to be trained separately for different time windows, or extended with temporally dynamic land-cover information such as site-specific crop calendars. Likewise, for long observational records, partitioning performance may further improve when training is conducted separately for shorter temporal periods, in order to account for gradual changes in ecosystem functioning caused by disturbances, management practices, or long-term CO_2 fertilization effects (Ainsworth and Long, 2005). This aspect will be investigated more systematically in future work.

Particular emphasis should also be placed on improving the representation of R_{eco}, which remains substantially more difficult to model than GPP. Respiration is strongly influenced by processes that are not directly observable from satellite data, including variations in soil carbon pools and legacy effects of antecedent meteorological conditions (Subke and Bahn, 2010). Some studies have suggested that modelling ecosystem respiration with recurrent neural networks may improve the representation of temporal dependencies and lagged responses to temperature and moisture variability (Kraft et al., 2019).

The neural-network framework presented here has been implemented within the `pyVPRM` package (Glauch et al., 2025) and is openly available to the scientific community. The framework is designed to unify three related applications: (i) partitioning of NEE, (ii) interpretation of latent meteorological controls, and (iii) carbon-flux upscaling. Integration into `pyVPRM` enables the consistent exploitation of all available spatiotemporal information across these applications. The `pyVPRM` repository also contains example code to run our partitioning approach with data files following the standard of the FLUXNET Shuttle Catalog and the FLUXNET Data Explorer (Keenan, 2026).

Although the present study focuses on flux partitioning, future work will investigate the remaining two use cases in greater detail. We anticipate that this framework will provide new insights into the temperature and humidity dependence of GPP and ecosystem respiration, thereby informing the development of process-based biosphere models. Ultimately, this work represents a step toward a fully Sentinel-2-based CO_2 flux upscaling framework, by applying the trained networks to sufficiently similar ecosystems and enabling extrapolation from site observations to local, continental, and potentially global scales.

Code and data availability. The current versions of pyVPRM and `pyVPRNN_v1` are available from the project website: https://github.com/tglauch/pyVPRM under the MIT licence. The exact version of the model used to produce the results used in this paper is archived on Zenodo https://zenodo.org/records/21710227 (v6.0.1). Ecosystem final quality (L2) product in ETC-Archive format - INTERIM release 2025-1 were downloaded from the ICOS Carbon portal, DOI: https://doi.org/10.18160/S6HM-CP8Q. Sentinel-2 Collection 1 Level-2A data are distributed through the Copernicus Data Space Ecosystem (ESA, 2022). The Copernicus dynamic land-cover map is accessible through https://doi.org/10.5281/zenodo.3939049 (Copernicus Land Cover Service).

https://doi.org/10.5194/egusphere-2026-4847
Preprint. Discussion started: 24 August 2026

Appendix A: Flux footprints

A1 Full footprint equation

The FFP footprint parameterization was developed by Kljun et al. (2015b).

The parameter σ_y of the Gaussian crosswind dispersion in Eq. 5 is defined as

$$\sigma_y = \frac{\sigma_y^* z_m \sigma_v}{p_{s1} u^*} \tag{A1}$$

Here, the parameters p_{s1} and σ_y^* are defined as

$$p_{s1} = \begin{cases} \min(1, |\frac{z_m}{L}|^{-1} 10^{-}5 + 0.8) & \text{for } L < 0 \\ \min(1, |\frac{z_m}{L}|^{-1} 10^{-}5 + 0.55) & \text{for } L > 0 \end{cases} \tag{A2}$$

and

$$\sigma_y^* = a_c \sqrt{\frac{b_c {X^*}^2}{1 + c_c X^*}} \tag{A3}$$

with parameters $a_c = 2.17$, $b_c = 1.66$ and $c_c = 20.0$.

The non-dimensional upwind distance in the along-wind distribution in Eq. 6 is defined as

$$X^* = \frac{x}{z_m} \left(1 - \frac{z_m}{h}\right) \frac{u^*}{u\, k}. \tag{A4}$$

The parameters used in the along-wind distribution in Eq. 6 are $a = 1.452$, $b = -1.991$, $c = 1.462$ and $d = 0.136$.

A2 Determining zero-plane displacement for the footprint calculation

The measurement height z_m used in the FFP footprint model is not the height of the measurement above the ground, z_{sensor}, but above the zero-plane displacement height d, where $z_m = z_{\text{sensor}} - d$. Of these three heights, only z_{sensor} is available in the metadata of the flux towers. However, if both L and z_L are available, the measurement height can be calculated from $z_m = z_L L$, to recover the measurement height that was assumed during the generation of the flux data set. From the metadata of the sites, we take time intervals of fixed z_{sensor} and over these intervals average the recovered z_m. These time intervals are necessary, as for some of the sites, the sensors are occasionally moved in height. the If z_L is missing for an eddy covariance site, we manually choose a canopy height z_{canopy} based on the documented vegetation heights or the site report. Then d can be estimated as $d = 0.67 z_{\text{canopy}}$.

A3 Regridding calculated footprints

The footprints are calculated in a local tangent plane coordinate system (x, y) on a higher resolution grid, with the x-axis pointing east and the y-axis pointing north. The footprints then need to be regridded to the lower spatial resolution of the

https://doi.org/10.5194/egusphere-2026-4847
Preprint. Discussion started: 24 August 2026

satellite grid. We use the `xESMF` package of Zhuang et al. (2023). To be able to use the same regridder weights for all measurements of one site, we take the same high-resolution footprint grid for each time step. To obtain the footprint in the correct wind direction, we first rotate the grid anti-clockwise by the wind direction, then calculate the footprint, and then rotate the grid back into its standard position. The center and corner locations of the calculation grid have to be given in latitude, longitude values to the regridder. For the local footprint grid, the point of tangency is at the flux tower location (latitude, longitude, zero-plane elevation above sea). In the first transformation step the coordinates are converted to a geocentric earth-centered, earth-fixed coordinate system. In the second transformation step, the coordinates are converted to a geodetic (latitude, longitude, elevation) representation. We use the proj (PROJ contributors, 2026) string

```
+proj=pipeline +step +inv +proj=topocentric +lon_0={lon}
+lat_0={lat} +h_0={elev} +step +inv +proj=cart
+ellps=WGS84
```

to perform this transformation on the grid center and corner locations.

https://doi.org/10.5194/egusphere-2026-4847
Preprint. Discussion started: 24 August 2026

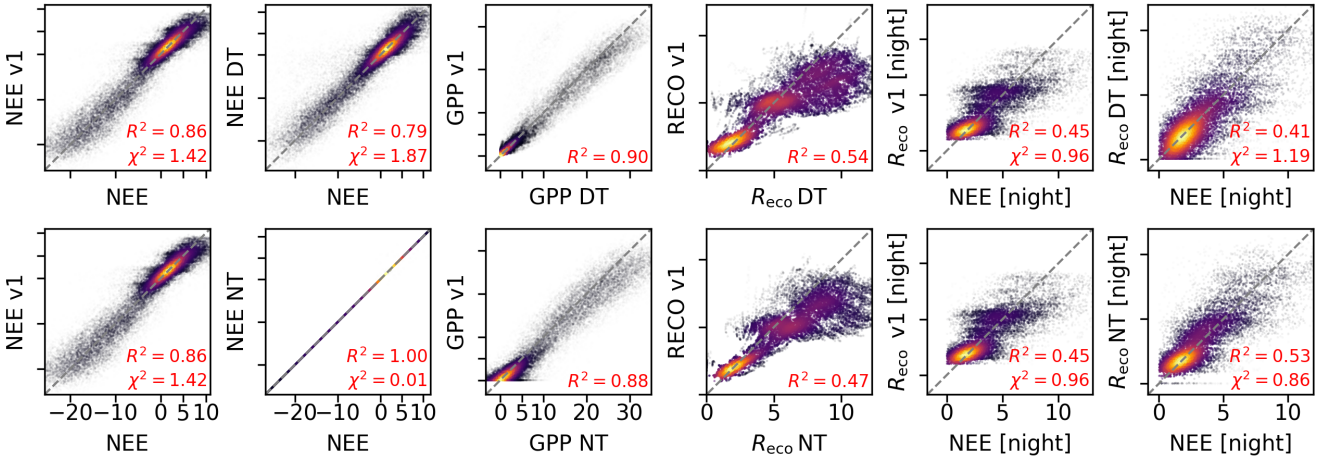

Figure A1. Scatter plots comparing different partitioning approaches (`pyVPRNN_v1`, nighttime (NT) partitioning, and daytime (DT) partitioning) against each other and against observations at the ICOS site DK-Sor. The top row shows comparisons relative to DT partitioning, while the bottom row shows comparisons relative to NT partitioning. Colors indicate point density. Abbreviations are as follows: Obs. = observations, v1 = `pyVPRNN_v1`, DT = day-time partitioning, NT = night-time partitioning. All fluxes are given in units of μmol CO_2 m^{-2} s^{-1}.The x- and y-axes share the same limits and tick intervals in all cases.

https://doi.org/10.5194/egusphere-2026-4847
Preprint. Discussion started: 24 August 2026

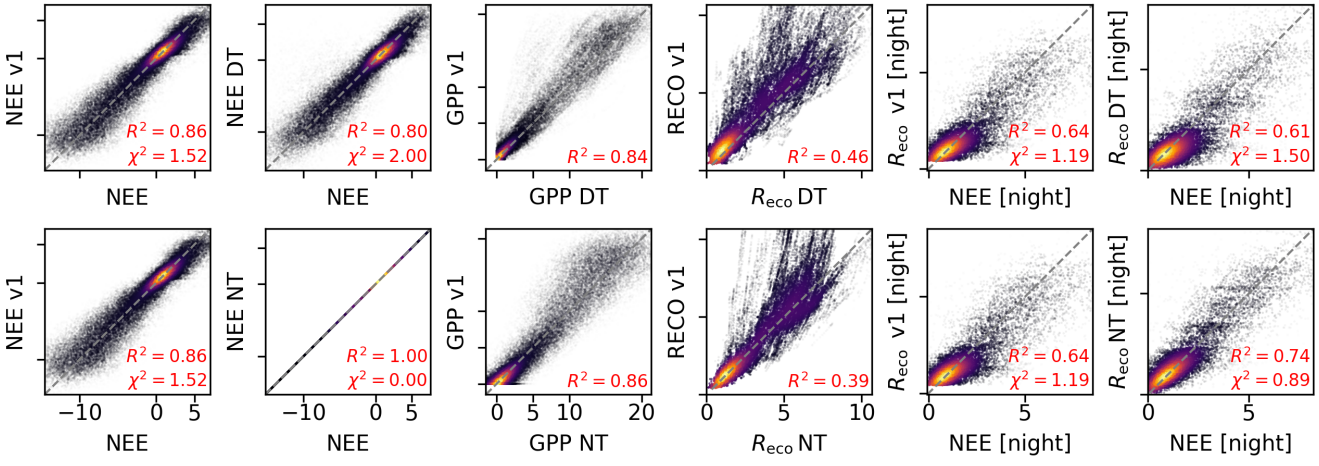

Figure A2. Scatter plots comparing different partitioning approaches (`pyVPRNN_v1`, night-time (NT) partitioning, and day-time (DT) partitioning) against each other and against observations at the ICOS site SE-Svb. The top row shows comparisons relative to DT partitioning, while the bottom row shows comparisons relative to NT partitioning. Colors indicate point density. Abbreviations are as follows: Obs. = observations, v1 = `pyVPRNN_v1`, DT = day-time partitioning, NT = night-time partitioning. All fluxes are given in units of μmol CO_2 m^{-2} s^{-1}.The x- and y-axes share the same limits and tick intervals in all cases.

https://doi.org/10.5194/egusphere-2026-4847
Preprint. Discussion started: 24 August 2026

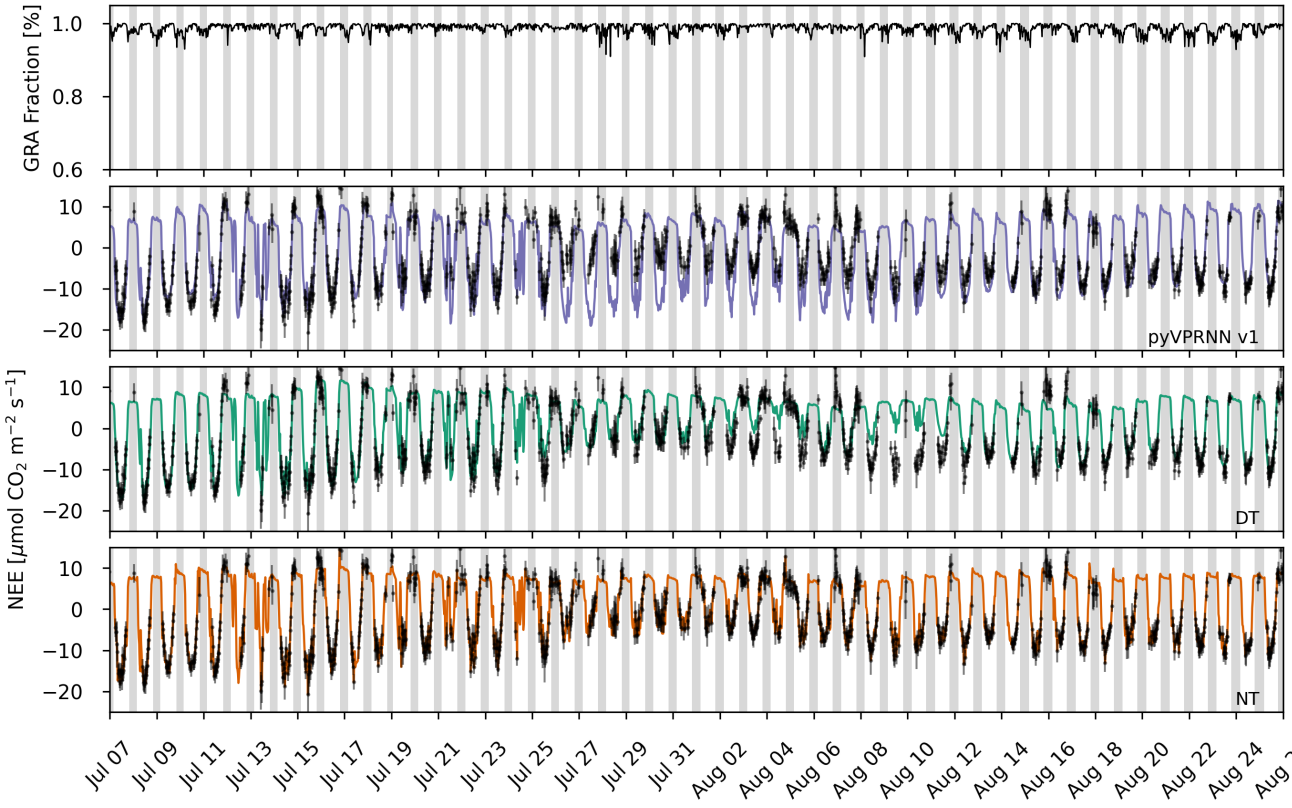

Figure A3. Half-hourly time series at DK-Sor between 7 July and 26 August 2024. The top panel shows the fraction of grassland within the tower footprint. The three panels below show NEE as estimated by `pyVPRNN_v1`, DT partitioning, and NT partitioning, respectively. Measured data (NEE_VUT_REF_QC = 0) are shown with 1σ error bars. Shaded areas indicate nighttime. Note that for NT partitioning, the nighttime flux shown is R_{eco} with GPP set to zero by construction.

https://doi.org/10.5194/egusphere-2026-4847
Preprint. Discussion started: 24 August 2026

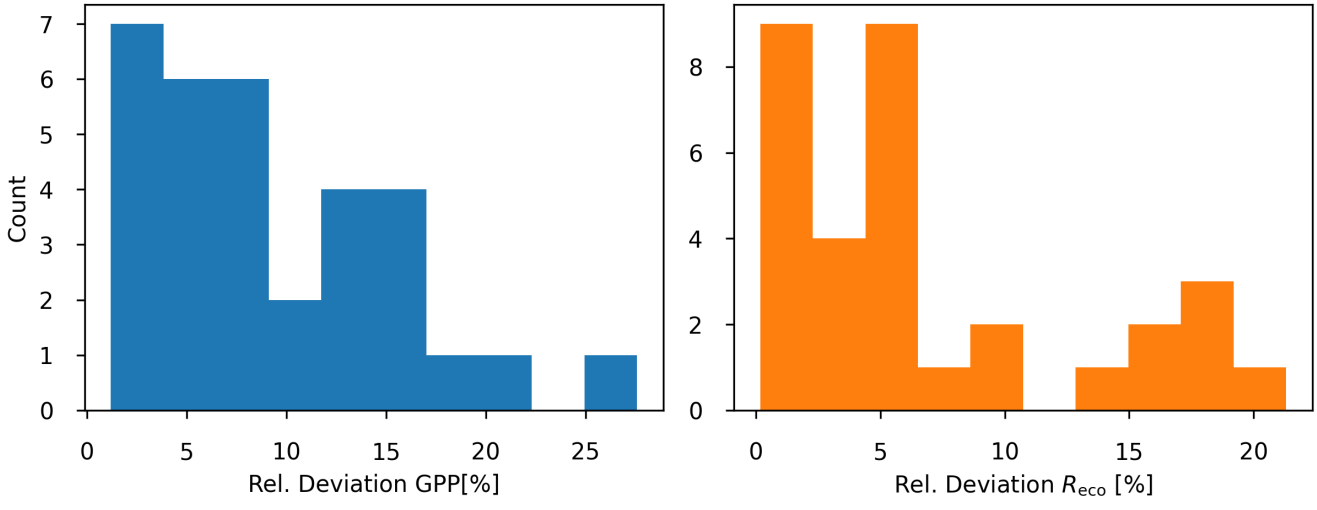

Figure A4. Histogram of the average relative deviation for GPP (left) and R_{eco} (right) when using the footprint in flux inference (measured flux) and assuming a steady footprint 100m × 100m around the tower location (ecosystem flux) for the 32 sites included in this study.

https://doi.org/10.5194/egusphere-2026-4847
Preprint. Discussion started: 24 August 2026

Table A1. Overview of the network architecture for `pyVPRNN_v1` including layer roles and number of trainable parameters. H and W represent the height and width of the input images.

Component	Layer	Description	# of parameters
Inputs			
Satellite input	Input	$(H, W, 3)$	0
Static input	Input	$(H, W, 9)$: land-cover + NIRv percentiles	0
Meteorology input	Input	$(H, W, 5)$	0
Potential radiation	Input	$(H, W, 1)$: SW_IN_POT	0
Footprint input	Input	(H, W)	0
Flux mask	Input	(H, W)	0
Feature selection and broadcast			
met_gpp	SelectFeatures	Select 4 met variables for GPP	0
met_reco	SelectFeatures	Select 3 met variables for R_{eco}	0
sat_static_concat	Concatenate	Combine sat + static as reference shape	0
Broadcast to image	BroadcastToImage	Tile met fields to satellite resolution	0
GPP branch			
gpp_concat	Concatenate	Combine 3 sat + 9 static + 4 met = 16 channels	0
Conv2D (1)	Conv2D	32 filters, input 16 channels	544
Conv2D (2–6)	Conv2D $\times 5$	32$\rightarrow$32 softplus layers	$5 \times 1056 = 5280$
GPP output map	Conv2D	1 filter, bias init = 0.3	33
GPPPenalty	GPPPenalty	Non-trainable physics constraint (GPP ceiling)	0
Day mask	DayMask	Mask nighttime using SW_IN_POT	0
Footprint weighting	Multiply	Apply footprint weights	0
Global pooling	GlobalSumPooling	Aggregate GPP map to scalar	0
R_{eco} **branch**			
reco_concat	Concatenate	Combine 3 sat + 9 static + 3 met = 15 channels	0
Conv2D (1)	Conv2D	32 filters, input 15 channels	512
Conv2D (2–6)	Conv2D $\times 5$	32$\rightarrow$32 softplus layers	$5 \times 1056 = 5280$
RECO output map	Conv2D	1 filter, bias init = 0.7	33
TimeIntegratedRatioPenalty	TimeIntegratedRatioPenalty	Consistency constraint discouraging R_{eco} from exceeding GPP by more than a fixed ratio	0
Footprint weighting	Multiply	Apply footprint weights	0
Global pooling	GlobalSumPooling	Aggregate R_{eco} map to scalar	0
NEE output (physics constraint)			
NEE = R_{eco} – GPP	Subtract	Physics-motivated flux combination	0
Total trainable parameters			**11,682**

https://doi.org/10.5194/egusphere-2026-4847
Preprint. Discussion started: 24 August 2026

Table A2. Nighttime (NT) partitioning and `pyVPRNN_v1` (v1) evaluation metrics. Entries show R^2 or R^2 (χ^2) where available; '–' indicates a comparison that was not computed or is not meaningful (NT's daytime NEE comparison is tautological by construction and therefore omitted – see main text). The unshaded GPP/R_{eco} NT/v1 columns compare the NT reference product directly against `pyVPRNN_v1` predictions and carry no χ^2, since this is a method-vs-method comparison, not a comparison against observed NEE with a defined uncertainty.

Site	Veg.	NEE v1 [day]	NEE NT [day]	GPP NT/v1 [day]	R_{eco} NT/v1	NEE v1 [night]	NEE NT [night]
BE-Bra	ENF	0.78 (1.17)	–	0.81	0.74	0.12 (0.82)	0.16 (0.76)
BE-Dor	GRA	0.79 (2.53)	–	0.80	0.81	0.68 (2.22)	0.85 (0.90)
CH-Dav	ENF	0.60 (1.76)	–	0.65	0.61	0.14 (1.33)	0.23 (1.28)
CZ-BK1	ENF	0.70 (2.73)	–	0.64	0.02	0.21 (1.58)	0.52 (1.39)
CZ-Lnz	DBF	0.75 (1.21)	–	0.80	0.79	0.17 (0.96)	0.20 (0.93)
DE-HoH	DBF	0.74 (1.54)	–	0.77	0.62	0.26 (1.03)	0.32 (0.96)
DE-RuR	GRA	0.58 (4.43)	–	0.59	0.51	0.55 (2.30)	0.71 (1.08)
DE-RuW	ENF	0.59 (2.37)	–	0.40	0.21	0.22 (2.44)	0.41 (1.87)
DE-Tha	ENF	0.60 (2.63)	–	0.64	0.69	0.35 (1.06)	0.42 (0.97)
DK-RCW	DBF	0.90 (1.96)	–	0.92	0.82	0.61 (2.32)	0.73 (0.98)
DK-Sor	DBF	0.82 (1.68)	–	0.80	0.52	0.43 (1.10)	0.52 (0.98)
FI-Hyy	ENF	0.80 (2.31)	–	0.84	0.78	0.66 (1.32)	0.74 (1.00)
FI-Sod	ENF	0.83 (2.44)	–	0.78	0.58	0.78 (1.64)	0.85 (1.75)
FR-Bil	ENF	0.79 (2.40)	–	0.74	0.32	0.40 (1.32)	0.55 (0.94)
FR-CLt	GRA	0.51 (5.27)	–	0.53	0.49	0.28 (2.80)	0.49 (1.31)
FR-FBn	ENF	0.80 (2.73)	–	0.71	0.14	0.29 (1.61)	0.47 (0.98)
FR-Fon	DBF	0.72 (1.38)	–	0.75	0.47	0.08 (1.01)	0.15 (0.95)
FR-Hes	DBF	0.81 (1.45)	–	0.80	0.24	0.18 (0.93)	0.19 (1.01)
FR-Lqu	GRA	0.82 (3.15)	–	0.85	0.81	0.72 (1.99)	0.79 (1.58)
FR-Lus	GRA	0.76 (4.99)	–	0.73	0.50	0.61 (2.65)	0.85 (1.05)
FR-Mej	GRA	0.65 (2.68)	–	0.64	0.46	0.35 (2.02)	0.64 (1.01)
FR-Pue	EBF	0.75 (3.66)	–	0.64	0.22	0.37 (1.45)	0.58 (1.00)
FR-Tou	GRA	0.81 (2.38)	–	0.81	0.60	0.39 (1.77)	0.58 (1.18)
GL-ZaH	GRA	0.58 (8.82)	–	0.56	-0.07	0.09 (3.09)	0.12 (5.36)
IT-MBo	GRA	0.78 (3.03)	–	0.87	0.92	0.81 (1.40)	0.86 (1.01)
IT-Ren	ENF	0.68 (3.53)	–	0.72	0.57	0.32 (1.54)	0.45 (1.24)
IT-SR2	ENF	0.63 (2.07)	–	0.61	0.51	0.22 (1.44)	0.44 (0.93)
NL-Loo	ENF	0.75 (1.22)	–	0.80	0.82	0.14 (1.00)	0.18 (0.94)
NO-Hur	ENF	0.08 (1.69)	–	0.31	0.65	0.25 (1.15)	0.32 (1.00)
SE-Htm	ENF	0.79 (1.71)	–	0.75	0.60	0.58 (1.25)	0.69 (1.08)
SE-Nor	ENF	0.84 (1.39)	–	-0.19	0.14	0.55 (1.31)	0.23 (1.82)
SE-Svb	ENF	0.82 (1.63)	–	0.83	0.73	0.65 (1.24)	0.74 (0.95)

https://doi.org/10.5194/egusphere-2026-4847
Preprint. Discussion started: 24 August 2026

Table A3. Daytime (DT) partitioning and `pyVPRNN_v1` (v1) evaluation metrics. Entries show R^2 or R^2 (χ^2) where available; '–' indicates a comparison that was not computed or is not meaningful. The unshaded GPP/R_{eco} DT/v1 columns compare the DT reference product directly against `pyVPRNN_v1` predictions and carry no χ^2, since this is a method-vs-method comparison, not a comparison against observed NEE with a defined uncertainty.

Site	Veg.	NEE v1 [day]	NEE DT [day]	GPP DT/v1 [day]	R_{eco} DT/v1	NEE v1 [night]	NEE DT [night]
BE-Bra	ENF	0.78 (1.17)	0.77 (1.33)	0.82	0.39	0.12 (0.82)	-0.03 (1.08)
BE-Dor	GRA	0.79 (2.53)	0.64 (3.98)	0.72	0.71	0.68 (2.22)	0.73 (2.03)
CH-Dav	ENF	0.60 (1.76)	0.59 (2.23)	0.75	0.43	0.14 (1.33)	0.06 (1.62)
CZ-BK1	ENF	0.70 (2.73)	0.66 (4.05)	0.70	0.13	0.21 (1.58)	0.27 (2.54)
CZ-Lnz	DBF	0.75 (1.21)	0.77 (1.15)	0.89	0.45	0.17 (0.96)	0.07 (1.13)
DE-HoH	DBF	0.74 (1.54)	0.71 (1.72)	0.83	0.50	0.26 (1.03)	0.20 (1.28)
DE-RuR	GRA	0.58 (4.43)	0.73 (2.45)	0.59	0.58	0.55 (2.30)	0.61 (2.16)
DE-RuW	ENF	0.59 (2.37)	–	–	–	0.22 (2.44)	–
DE-Tha	ENF	0.60 (2.63)	0.64 (2.68)	0.77	0.43	0.35 (1.06)	0.07 (1.90)
DK-RCW	DBF	0.90 (1.96)	0.74 (3.73)	0.82	0.76	0.61 (2.32)	0.69 (1.72)
DK-Sor	DBF	0.82 (1.68)	0.70 (2.28)	0.82	0.57	0.43 (1.10)	0.42 (1.29)
FI-Hyy	ENF	0.80 (2.31)	0.81 (2.15)	0.85	0.68	0.66 (1.32)	0.62 (1.76)
FI-Sod	ENF	0.83 (2.44)	0.80 (2.86)	0.78	0.66	0.78 (1.64)	0.78 (2.23)
FR-Bil	ENF	0.79 (2.40)	0.78 (2.49)	0.68	0.21	0.40 (1.32)	0.35 (1.51)
FR-CLt	GRA	0.51 (5.27)	0.73 (4.89)	0.55	0.43	0.28 (2.80)	0.35 (2.40)
FR-FBn	ENF	0.80 (2.73)	0.84 (1.68)	0.68	0.13	0.29 (1.61)	0.21 (1.76)
FR-Fon	DBF	0.72 (1.38)	0.72 (1.37)	0.85	0.34	0.08 (1.01)	-0.01 (1.17)
FR-Hes	DBF	0.81 (1.45)	0.77 (1.87)	0.86	0.43	0.18 (0.93)	0.10 (1.07)
FR-Lqu	GRA	0.82 (3.15)	0.78 (3.38)	0.82	0.72	0.72 (1.99)	0.68 (2.82)
FR-Lus	GRA	0.76 (4.99)	0.78 (2.80)	0.61	0.53	0.61 (2.65)	0.79 (1.54)
FR-Mej	GRA	0.65 (2.68)	0.79 (1.68)	0.67	0.51	0.35 (2.02)	0.52 (1.67)
FR-Pue	EBF	0.75 (3.66)	0.81 (2.25)	0.65	0.26	0.37 (1.45)	0.29 (2.08)
FR-Tou	GRA	0.81 (2.38)	0.84 (1.67)	0.77	0.46	0.39 (1.77)	0.31 (2.56)
GL-ZaH	GRA	0.58 (8.82)	–	–	–	0.09 (3.09)	–
IT-MBo	GRA	0.78 (3.03)	0.81 (2.87)	0.72	0.72	0.81 (1.40)	0.76 (1.60)
IT-Ren	ENF	0.68 (3.53)	0.66 (4.11)	0.73	0.55	0.32 (1.54)	0.28 (2.08)
IT-SR2	ENF	0.63 (2.07)	0.66 (1.83)	0.72	0.36	0.22 (1.44)	0.23 (1.47)
NL-Loo	ENF	0.75 (1.22)	0.70 (1.55)	0.86	0.66	0.14 (1.00)	0.03 (1.14)
NO-Hur	ENF	0.08 (1.69)	–	–	–	0.25 (1.15)	–
SE-Htm	ENF	0.79 (1.71)	0.64 (2.75)	0.72	0.51	0.58 (1.25)	0.55 (1.49)
SE-Nor	ENF	0.84 (1.39)	0.08 (7.83)	-0.38	0.11	0.55 (1.31)	0.23 (2.15)
SE-Svb	ENF	0.82 (1.63)	0.72 (2.23)	0.79	0.70	0.65 (1.24)	0.61 (1.56)

https://doi.org/10.5194/egusphere-2026-4847
Preprint. Discussion started: 24 August 2026

Author contributions. TG developed and implemented the software framework *pyVPRNN* and performed the analysis. MK designed the implementation of the tower footprints and worked on the data analysis. SV, SB, AB, and JM supervised the work. All authors participated in the interpretation of the results and in the writing and editing of the publication.

Competing interests. The contact author has declared that none of the authors has any competing interests.

Acknowledgements. The authors gratefully acknowledge the computational and data resources provided by the Leibniz Supercomputing Centre through the Terrabyte facilities. We acknowledge the following ICOS ecosystem stations for the eddy-covariance data used in this study: BE-Bra, BE-Dor, CH-Dav, CZ-BK1, CZ-Lnz, DE-HoH, DE-RuR, DE-RuW, DE-Tha, DK-RCW, DK-Sor, FI-Hyy, FI-Sod, FR-Bil, FR-CLt, FR-FBn, FR-Fon, FR-Hes, FR-Lqu, FR-Lus, FR-Mej, FR-Pue, FR-Tou, GL-ZaH, IT-MBo, IT-Ren, IT-SR2, NL-Loo, NO-Hur, SE-Htm, SE-Nor, and SE-Svb. We further acknowledge the Integrated Carbon Observation System (ICOS) Research Infrastructure for the provision of data, processing, and guidance. The work was financed through the CO2KI project of the BMBF (project number FZK50EE2212).

https://doi.org/10.5194/egusphere-2026-4847
Preprint. Discussion started: 24 August 2026

References

Ainsworth, E. A. and Long, S. P.: What have we learned from 15 years of free-air CO2 enrichment (FACE)? A meta-analytic review of the responses of photosynthesis, canopy properties and plant production to rising CO2, New phytologist, 165, 351–372, 2005.

Alladi, H. K., Sandeep, A., P., P., and Bv, B.: Evaluation of ERA5 boundary layer height against radiosonde measurements: Regional drivers, spatiotemporal variability, and trends over the Indian Monsoon Region, Atmospheric Research, 329, 108 511, https://doi.org/https://doi.org/10.1016/j.atmosres.2025.108511, 2026.

Atkin, O. K. and Tjoelker, M. G.: Thermal acclimation and the dynamic response of plant respiration to temperature, Trends in Plant Science, 8, 343–351, https://doi.org/https://doi.org/10.1016/S1360-1385(03)00136-5, 2003.

Aubinet, M., Berbigier, P., Bernhofer, C., Cescatti, A., Feigenwinter, C., Granier, A., Grünwald, T., Havrankova, K., Heinesch, B., Longdoz, B., Marcolla, B., Montagnani, L., and Sedlak, P.: Comparing CO2 Storage and Advection Conditions at Night at Different Carboeuroflux Sites, Boundary-Layer Meteorology, 116, 63–93, https://doi.org/10.1007/s10546-004-7091-8, 2005.

Aubinet, M., Vesala, T., and Papale, D.: Eddy covariance: a practical guide to measurement and data analysis, Springer Science & Business Media, 2012.

Badgley, G., Field, C. B., and Berry, J. A.: Canopy near-infrared reflectance and terrestrial photosynthesis, Science advances, 3, e1602 244, 2017.

Baldocchi, D., Falge, E., Gu, L., Olson, R., Hollinger, D., Running, S., Anthoni, P., Bernhofer, C., Davis, K., Evans, R., et al.: FLUXNET: A new tool to study the temporal and spatial variability of ecosystem-scale carbon dioxide, water vapor, and energy flux densities, Bulletin of the American Meteorological society, 82, 2415–2434, 2001.

Baldocchi, D. D.: Assessing the eddy covariance technique for evaluating carbon dioxide exchange rates of ecosystems: past, present and future, Global Change Biology, 9, 479–492, https://doi.org/https://doi.org/10.1046/j.1365-2486.2003.00629.x, 2003.

Bonan, G., Williams, M., Fisher, R., and Oleson, K.: Modeling stomatal conductance in the earth system: linking leaf water-use efficiency and water transport along the soil–plant–atmosphere continuum, Geoscientific Model Development, 7, 2193–2222, 2014.

Chu, H., Baldocchi, D. D., John, R., Wolf, S., and Reichstein, M.: Fluxes all of the time? A primer on the temporal representativeness of FLUXNET, Journal of Geophysical Research: Biogeosciences, 122, 289–307, https://doi.org/https://doi.org/10.1002/2016JG003576, 2017.

Chu, H., Luo, X., Ouyang, Z., Chan, W. S., Dengel, S., Biraud, S. C., Torn, M. S., Metzger, S., Kumar, J., Arain, M. A., Arkebauer, T. J., Baldocchi, D., Bernacchi, C., Billesbach, D., Black, T. A., Blanken, P. D., Bohrer, G., Bracho, R., Brown, S., Brunsell, N. A., Chen, J., Chen, X., Clark, K., Desai, A. R., Duman, T., Durden, D., Fares, S., Forbrich, I., Gamon, J. A., Gough, C. M., Griffis, T., Helbig, M., Hollinger, D., Humphreys, E., Ikawa, H., Iwata, H., Ju, Y., Knowles, J. F., Knox, S. H., Kobayashi, H., Kolb, T., Law, B., Lee, X., Litvak, M., Liu, H., Munger, J. W., Noormets, A., Novick, K., Oberbauer, S. F., Oechel, W., Oikawa, P., Papuga, S. A., Pendall, E., Prajapati, P., Prueger, J., Quinton, W. L., Richardson, A. D., Russell, E. S., Scott, R. L., Starr, G., Staebler, R., Stoy, P. C., Stuart-Haëntjens, E., Sonnentag, O., Sullivan, R. C., Suyker, A., Ueyama, M., Vargas, R., Wood, J. D., and Zona, D.: Representativeness of Eddy-Covariance flux footprints for areas surrounding AmeriFlux sites, Agricultural and Forest Meteorology, 301-302, 108 350, https://doi.org/https://doi.org/10.1016/j.agrformet.2021.108350, 2021.

Chu, H., Metzger, S., Ouyang, Z., Griebel, A., Yi, K., Durden, D., Wolf, S., Kasak, K., Rey-Sanchez, C., Hernandez Rodriguez, L. C., Oikawa, P., Falco, N., Runkle, B. R. K., Ahmadi, A., and Matthes, J.: Flux Footprints: A Critical Link to Bridge

https://doi.org/10.5194/egusphere-2026-4847
Preprint. Discussion started: 24 August 2026

Eddy-Covariance Measurements With Models, Remote Sensing, and Other Observations, Global Change Biology, 32, e70 887, https://doi.org/https://doi.org/10.1111/gcb.70887, e70887 GCB-25-2428.R1, 2026.

Copernicus Land Monitoring Service: Copernicus Global Land Service Dynamic Land Cover 100 m (v3), https://land.copernicus.eu/en/products/global-dynamic-land-cover/copernicus-global-land-service-land-cover-100m-collection-3-epoch-2015-2019-globe, accessed 2026, includes global annual land cover maps at 100 m resolution, 2019.

Copernicus Land Monitoring Service: Copernicus Global Land Service Dynamic Land Cover 10 m (v1), https://documentation.dataspace.copernicus.eu/APIs/SentinelHub/Data/clms/land-cover-and-land-use-mapping/global-dynamic-land-cover/lcm_global_10m_yearly_v1.html, accessed 2026, global 10m land cover map built from Sentinel data, 2025.

Drusch, M., Del Bello, U., Carlier, S., Colin, O., Fernandez, V., Gascon, F., Hoersch, B., Isola, C., Laberinti, P., Martimort, P., et al.: Sentinel-2: ESA's optical high-resolution mission for GMES operational services, Remote sensing of Environment, 120, 25–36, 2012.

ESA: Sentinel-2 MSI Level-2A BOA Reflectance, https://doi.org/10.5270/s2_-znk9xsj, 2022.

Falge, E., Baldocchi, D., Olson, R., Anthoni, P., Aubinet, M., Bernhofer, C., Burba, G., Ceulemans, R., Clement, R., Dolman, H., et al.: Gap filling strategies for defensible annual sums of net ecosystem exchange, Agricultural and forest meteorology, 107, 43–69, 2001.

Farquhar, G. D., von Caemmerer, S. v., and Berry, J. A.: A biochemical model of photosynthetic CO2 assimilation in leaves of C3 species, planta, 149, 78–90, 1980.

Gaber, M., Kang, Y., Schurgers, G., and Keenan, T.: Using automated machine learning for the upscaling of gross primary productivity, Biogeosciences, 21, 2447–2472, https://doi.org/10.5194/bg-21-2447-2024, 2024.

Gao, B.-C.: NDWI—A normalized difference water index for remote sensing of vegetation liquid water from space, Remote sensing of environment, 58, 257–266, 1996.

Gitelson, A. A., Viña, A., Ciganda, V., Rundquist, D. C., and Arkebauer, T. J.: Remote estimation of canopy chlorophyll content in crops, Geophysical research letters, 32, 2005.

Glauch, T., Marshall, J., Gerbig, C., Botía, S., Gałkowski, M., Vardag, S. N., and Butz, A.: pyVPRM: A next-generation Vegetation Photosynthesis and Respiration Model for the post-MODIS era, Geoscientific Model Development, 18, 4713–4742, 2025.

Goodfellow, I., Bengio, Y., Courville, A., and Bengio, Y.: Deep learning, vol. 1, MIT press Cambridge, 2016.

Gu, L., Falge, E. M., Boden, T., Baldocchi, D. D., Black, T., Saleska, S. R., Suni, T., Verma, S. B., Vesala, T., Wofsy, S. C., and Xu, L.: Objective threshold determination for nighttime eddy flux filtering, Agricultural and Forest Meteorology, 128, 179–197, https://doi.org/https://doi.org/10.1016/j.agrformet.2004.11.006, 2005.

Guanter, L., Zhang, Y., Jung, M., Joiner, J., Voigt, M., Berry, J. A., Frankenberg, C., Huete, A. R., Zarco-Tejada, P., Lee, J.-E., et al.: Global and time-resolved monitoring of crop photosynthesis with chlorophyll fluorescence, Proceedings of the National Academy of Sciences, 111, E1327–E1333, 2014.

Heidbach, K., Schmid, H. P., and Mauder, M.: Experimental evaluation of flux footprint models, Agricultural and Forest Meteorology, 246, 142–153, https://doi.org/10.1016/j.agrformet.2017.06.008, 2017.

Hird, J. N. and McDermid, G. J.: Noise reduction of NDVI time series: An empirical comparison of selected techniques, Remote Sensing of Environment, 113, 248–258, 2009.

Hollinger, D. Y. and Richardson, A. D.: Uncertainty in eddy covariance measurements and its application to physiological models, Tree Physiology, 25, 873–885, https://doi.org/10.1093/treephys/25.7.873, 2005.

Horst, T. and Weil, J.: Footprint estimation for scalar flux measurements in the atmospheric surface layer, Boundary-Layer Meteorology, 59, 279–296, 1992.

https://doi.org/10.5194/egusphere-2026-4847
Preprint. Discussion started: 24 August 2026

Hsieh, C.-I., Katul, G., and Chi, T.-w.: An approximate analytical model for footprint estimation of scalar fluxes in thermally stratified atmospheric flows, Advances in Water Resources, 23, 765–772, https://doi.org/10.1016/S0309-1708(99)00042-1, 2000.

Huang, N., Niu, Z., Zhan, Y., Xu, S., Tappert, M. C., Wu, C., Huang, W., Gao, S., Hou, X., and Cai, D.: Relationships between soil respiration and photosynthesis-related spectral vegetation indices in two cropland ecosystems, Agricultural and Forest Meteorology, 160, 80–89, https://doi.org/https://doi.org/10.1016/j.agrformet.2012.03.005, 2012.

Ibrom, A., Lange Rønn, E., Lodsgaard Justesen, M., Møller, F., Pilegaard, K., and Schaarup Sørensen, J.: ETC L2 Fluxes from Soroe, 2020-12-31–2025-12-31, https://hdl.handle.net/11676/4TdixPcmYyo0Tp8CFomUiw7d, 2026.

Jiang, Y., Xu, J., Chu, C., Wu, X., and Zhang, B.: Different Driving Mechanisms for Spatial Variations in Soil Autotrophic and Heterotrophic Respiration: A Global Synthesis for Forest and Grassland Ecosystems, Agronomy, 16, https://doi.org/10.3390/agronomy16030372, 2026.

Jiang, Z., Huete, A. R., Didan, K., and Miura, T.: Development of a two-band enhanced vegetation index without a blue band, Remote sensing of Environment, 112, 3833–3845, 2008.

Ju, J., Zhou, Q., Freitag, B., Roy, D. P., Zhang, H. K., Sridhar, M., Mandel, J., Arab, S., Schmidt, G., Crawford, C. J., Gascon, F., Strobl, P. A., Masek, J. G., and Neigh, C. S.: The Harmonized Landsat and Sentinel-2 version 2.0 surface reflectance dataset, Remote Sensing of Environment, 324, 114 723, https://doi.org/https://doi.org/10.1016/j.rse.2025.114723, 2025.

Jung, M., Schwalm, C., Migliavacca, M., Walther, S., Camps-Valls, G., Koirala, S., Anthoni, P., Besnard, S., Bodesheim, P., Carvalhais, N., et al.: Scaling carbon fluxes from eddy covariance sites to globe: synthesis and evaluation of the FLUXCOM approach, Biogeosciences, 17, 1343–1365, 2020.

Karger, D. N., Conrad, O., Böhner, J., Kawohl, T., Kreft, H., Soria-Auza, R. W., Zimmermann, N. E., Linder, H. P., and Kessler, M.: Climatologies at high resolution for the earth's land surface areas, Scientific Data, 4, 170 122, https://doi.org/10.1038/sdata.2017.122, 2017.

Keenan, T., Baker, I., Barr, A., Ciais, P., Davis, K., Dietze, M., Dragoni, D., Gough, C. M., Grant, R., Hollinger, D., et al.: Terrestrial biosphere model performance for inter-annual variability of land-atmosphere CO2 exchange, Global Change Biology, 18, 1971–1987, 2012.

Keenan, T. F.: FLUXNET Data Explorer, https://doi.org/10.5281/zenodo.20331228, 2026.

Kljun, N., Calanca, P., Rotach, M., and Schmid, H. P.: A simple two-dimensional parameterisation for Flux Footprint Prediction (FFP), Geoscientific Model Development, 8, 3695–3713, 2015a.

Kljun, N., Calanca, P., Rotach, M. W., and Schmid, H. P.: A simple two-dimensional parameterisation for Flux Footprint Prediction (FFP), Geoscientific Model Development, 8, 3695–3713, https://doi.org/10.5194/gmd-8-3695-2015, 2015b.

Kormann, R. and Meixner, F. X.: An analytical footprint model for non-neutral stratification, Boundary-Layer Meteorology, 99, 207–224, 2001.

Kraft, B., Jung, M., Körner, M., Requena Mesa, C., Cortés, J., and Reichstein, M.: Identifying Dynamic Memory Effects on Vegetation State Using Recurrent Neural Networks, Frontiers in Big Data, Volume 2 - 2019, https://doi.org/10.3389/fdata.2019.00031, 2019.

Lasslop, G., Reichstein, M., Papale, D., Richardson, A. D., Arneth, A., Barr, A., Stoy, P., and Wohlfahrt, G.: Separation of net ecosystem exchange into assimilation and respiration using a light response curve approach: critical issues and global evaluation, Global change biology, 16, 187–208, 2010.

Leclerc, M. Y. and Foken, T.: Footprints in Micrometeorology and Ecology, Springer Berlin Heidelberg, Berlin, Heidelberg, https://doi.org/10.1007/978-3-642-54545-0, 2014.

Leuning, R.: A critical appraisal of a combined stomatal-photosynthesis model for C3 plants, Plant, Cell & Environment, 18, 339–355, 1995.

Lin, M., Chen, Q., and Yan, S.: Network in network, arXiv preprint arXiv:1312.4400, 2013.

https://doi.org/10.5194/egusphere-2026-4847
Preprint. Discussion started: 24 August 2026

Lloyd, J. and Taylor, J. A.: On the temperature dependence of soil respiration, Functional ecology, pp. 315–323, 1994.

Mahadevan, P., Wofsy, S. C., Matross, D. M., Xiao, X., Dunn, A. L., Lin, J. C., Gerbig, C., Munger, J. W., Chow, V. Y., and Gottlieb, E. W.: A satellite-based biosphere parameterization for net ecosystem CO2 exchange: Vegetation Photosynthesis and Respiration Model (VPRM), Global Biogeochemical Cycles, 22, 2008.

Mahecha, M. D., Reichstein, M., Carvalhais, N., Lasslop, G., Lange, H., Seneviratne, S. I., Vargas, R., Ammann, C., Arain, M. A., Cescatti, A., et al.: Global convergence in the temperature sensitivity of respiration at ecosystem level, Science, 329, 838–840, 2010.

Medlyn, B. E., Duursma, R. A., Eamus, D., Ellsworth, D. S., Prentice, I. C., Barton, C. V., Crous, K. Y., De Angelis, P., Freeman, M., and Wingate, L.: Reconciling the optimal and empirical approaches to modelling stomatal conductance, Global change biology, 17, 2134–2144, 2011.

Medlyn, B. E., De Kauwe, M. G., Lin, Y.-S., Knauer, J., Duursma, R. A., Williams, C. A., Arneth, A., Clement, R., Isaac, P., Limousin, J.-M., Linderson, M.-L., Meir, P., Martin-StPaul, N., and Wingate, L.: How do leaf and ecosystem measures of water-use efficiency compare?, New Phytologist, 216, 758–770, https://doi.org/10.1111/nph.14626, 2017.

Muñoz-Sabater, J., Dutra, E., Agustí-Panareda, A., Albergel, C., Arduini, G., Balsamo, G., Boussetta, S., Choulga, M., Harrigan, S., Hersbach, H., et al.: ERA5-Land: A state-of-the-art global reanalysis dataset for land applications, Earth system science data, 13, 4349–4383, 2021.

Niu, S., Chen, W., Liáng, L. L., Sierra, C. A., Xia, J., Wang, S., Heskel, M., Patel, K. F., Bond-Lamberty, B., Wang, J., Yvon-Durocher, G., Kirschbaum, M. U. F., Atkin, O. K., Huang, Y., Yu, G., and Luo, Y.: Temperature responses of ecosystem respiration, Nature Reviews Earth & Environment, 5, 559–571, https://doi.org/10.1038/s43017-024-00569-3, 2024a.

Niu, S., Chen, W., Liáng, L. L., Sierra, C. A., Xia, J., Wang, S., Heskel, M., Patel, K. F., Bond-Lamberty, B., Wang, J., et al.: Temperature responses of ecosystem respiration, Nature Reviews Earth & Environment, 5, 559–571, 2024b.

Novick, K. A., Biederman, J., Desai, A., Litvak, M., Moore, D. J., Scott, R., and Torn, M.: The AmeriFlux network: A coalition of the willing, Agricultural and Forest Meteorology, 249, 444–456, 2018.

Papale, D. and Valentini, R.: A new assessment of European forests carbon exchanges by eddy fluxes and artificial neural network spatialization, Global Change Biology, 9, 525–535, 2003.

Pastorello, G., Trotta, C., Canfora, E., Chu, H., Christianson, D., Cheah, Y.-W., Poindexter, C., Chen, J., Elbashandy, A., Humphrey, M., et al.: The FLUXNET2015 dataset and the ONEFlux processing pipeline for eddy covariance data, Scientific data, 7, 225, 2020.

Peichl, M., Nilsson, M., Larmanou, E., Smith, P., Marklund, P., De Simon, G., Lofvenius, P., Dignam, R., Holst, J., Molder, M., Andersson, T., Boschetti, F., Kozii, N., Linderson, M.-L., and Ottosson-Löfvenius, M.: ETC L2 Fluxes from Svartberget, 2018-12-31–2025-12-31, https://hdl.handle.net/11676/MCCzme--Xitf-2f2mKW-cd-m, 2026.

PROJ contributors: PROJ coordinate transformation software library, Open Source Geospatial Foundation, https://doi.org/10.5281/zenodo.5884394, 2026.

Ranjbar, S., Desai, A. R., Hoffman, S., Zahn, E., Bou-Zeid, E., and Stoy, P. C.: Constrained Carbon Partitioning: A Self-Trained Physics-Informed Machine Learning Model Refines GPP Estimates From Eddy Covariance Measurements, Global Change Biology, 32, e70 886, https://doi.org/https://doi.org/10.1111/gcb.70886, e70886 GCB-25-2427.R1, 2026.

Rebmann, C., Aubinet, M., Schmid, H., Arriga, N., Aurela, M., Burba, G., Clement, R., De Ligne, A., Fratini, G., Gielen, B., et al.: ICOS eddy covariance flux-station site setup: a review, International Agrophysics, 32, 471–494, 2018.

Reichstein, M., Rey, A., Freibauer, A., Tenhunen, J., Valentini, R., Banza, J., Casals, P., Cheng, Y., Grünzweig, J. M., Irvine, J., Joffre, R., Law, B. E., Loustau, D., Miglietta, F., Oechel, W., Ourcival, J.-M., Pereira, J. S., Peressotti, A., Ponti, F., Qi, Y., Rambal, S., Ray-

https://doi.org/10.5194/egusphere-2026-4847
Preprint. Discussion started: 24 August 2026

ment, M., Romanya, J., Rossi, F., Tedeschi, V., Tirone, G., Xu, M., and Yakir, D.: Modeling temporal and large-scale spatial variability of soil respiration from soil water availability, temperature and vegetation productivity indices, Global Biogeochemical Cycles, 17, https://doi.org/https://doi.org/10.1029/2003GB002035, 2003.

Reichstein, M., Falge, E., Baldocchi, D., Papale, D., Aubinet, M., Berbigier, P., Bernhofer, C., Buchmann, N., Gilmanov, T., Granier, A., et al.: On the separation of net ecosystem exchange into assimilation and ecosystem respiration: review and improved algorithm, Global change biology, 11, 1424–1439, 2005.

RI, I., Aalto, J., Aalto, P., Aaltonen, H., Aiguier, T., Akubia, J., Ala-Könni, J., Alivernini, A., Alonso, L., Aluome, C., Andersson, T., Arriga, N., Aurela, M., Brechet, L., Baab, F., Back, J., Bagheri, S., Baltes, U., Baneschi, I., Barral, H., Barten, S., Bastos Campos, F., Baur, T., Bauters, M., Bazot, S., Beauclair, P., Becker, N., Behrens, N., Belelli Marchesini, L., Bergström, G., Bernhofer, C., Berveiller, D., Biermann, T., Bignotti, L., Biron, R., Bloor, J., Bodson, B., Boeckx, P., Boeske, L., Bogaerts, G., Bonal, D., Boon, G., Bornet, F., Bortoli, M., Boschetti, F., Bosio, I., Bresseleers, S., Brut, A., Brümmer, C., Buchmann, N., Bulonza, E., Burban, B., Burri, S., Buysse, P., Båth, A., Calandrelli, D., Calvet, J.-C., Canut-Rocafort, G., Carrara, A., Cash, J., Cavagna, M., Ceschia, E., Chabbi, A., Chan, T., Chebbi, W., Chebil, B., Chianucci, F., Chipeaux, C., Chopin, H., Christen, A., Chrysoulakis, N., Claverie, N., Cobbe, I., Cohard, J.-M., Colosse, D., Conte, A., Corsanici, R., Coulaud, C., Courtois, P., Coyle, M., Cremonese, E., Crill, P., Cuntz, M., Cuocolo, D., Czerný, R., Depuydt, J., Daelman, R., Darenová, E., Darsonville, O., De Ligne, A., De Meulder, T., De Simon, G., Decau, M.-L., Dejosez, S., Dell'Acqua, A., Delorme, J.-P., Delpierre, N., Demoulin, L., Denou, J.-L., Di Tommasi, P., Dienstbach, L., Dignam, R., Dolfus, D., Domec, J.-C., Douxfils, B., Drösler, M., Drüe, C., Dufrêne, E., Dumont, B., Durand, B., Dusek, J., Eberl, J., Eichelmann, U., Ekili, D., Engelmann, T., Esposito, A., Esser, O., Etienne, J.-C., Etzold, S., Eugster, W., Famulari, D., Fares, S., Faurès, A., Fauvel, Y., Feigenwinter, C., Feigenwinter, I., Feldmann, I., Ferraris, D., Filippa, G., Fincham, W., Finco, A., Fischer, M., Flechard, C., Folino, G., Foltýnová, L., Foret, J., Foulquier, A., François, B., Friborg, T., Galliot, J.-N., Galvagno, M., Garcia Quiros, I., Garrigou, C., Gastal, F., Geilfus, N.-X., Gerosa, G., Gessler, A., Gharun, M., Giamberini, M., Gianelle, D., Gibrin, H., Gimper, S., Gioli, B., Girardin, C., Goded, I., Graf, A., Granouillac, F., Grehan, E., Grenier, M., Grudd, H., Grünwald, T., Guillot, T., Guzman, R., Hamon, Y., Harvey, D., Hatakka, J., Haustein, A., Hautmann, D., Hehn, M., Heinesch, B., Helfter, C., Heliasz, M., Herbst, M., Hildebrandt, A., Holst, J., Holst, T., Holtmann, A., Hortnagl, L., Hug, C., Huguet, C., Häni, M., Ibrom, A., Ilardi, F., Jackowicz-Korczynski, M. A., Jacotot, A., Janssens, I., Jensen, R., Jocher, G., Joetzjer, E., Jones, M., Järvi, L., Kalalian, C., Kempf, J., Kempka, P., Keronen, P., Kettler, M., Kimbesa, F., Kivalov, S., Klatt, J., Klimo, P., Kljun, N., Klumpp, K., Kogxylakis, G., Kolari, P., Kolbe, S., Korkiakoski, M., Korrensalo, A., Kowalska, N., Kozii, N., Krejza, J., Kristoffersson, A., Kruijt, B., Kruszewski, A., Kulmala, L., Kumar, S., Kummer, S., Laakso, H., Lafont, S., Lange, H., Lange Rønn, E., Larmanou, E., Laurila, T., Leeson, S., Lefevre, L., Lehner, I., Lemaire, B., Leonard, J., Levula, J., Levy, P., Liechti, K., Liger, L., Lily, J.-B., Limousin, J.-M., Linderson, M.-L., Lindgren, K., Lo Cascio, M., Lodsgaard Justesen, M., Lofvenius, P., Lohila, A., Longdoz, B., Lootens, R., Loubet, B., Loustau, D., Lucarini, A., Lundin, E., López, R., López-Blanco, E., Magliulo, V., Mammarella, I., Manco, A., Manise, T., Marcolla, B., Marek, M. V., Marklund, P., Marloie, O., Marras, S., Martin, R., Martin-Saint Paul, N., Marty, M., Martín, M. P., Marzuoli, R., Matilainen, T., Mattes, J., Matteucci, M., Mauder, M., Maurel, W., Mbifo, J., Meggio, F., Meier, F., Meier, P., Meire, A., Meis, J., Meissner, H., Mensah, C., Meyer, H., Michaud, L., Minerbi, S., Moderow, U., Molder, M., Montagnani, L., Moreno, G., Moretti, V., Morfin, A., Morra di Cella, U., Mullinger, N., Mäkelä, T., Männikkö, M., Männistö, E., Møller, F., Naiken, A., Naseer, M., Nemitz, E., Nezval, O., Nilsson, M., Norkko, J., Ocallaghan, F., Ojala, A., Orgun, A., Ottosson-Löfvenius, M., Ourcival, J.-M., Paasch, S., Paci, A., Pavelka, M., Pavot, L., Peichl, M., Peressotti, A., Perot-Guillaume, C., Perrot, C., Pihlatie, M., Pilegaard, K., Pilkottu, R., Piret, A., Pitacco, A., Plapp, T., Plebani, D., Politakos, K., Prasse, H., Provenzale, A., Pumpanen, J., Putzolu, S., Raco, B., Rainne, J., Rakos, N., Rebmann, C., Redepenning, D., Rinne, J., Rodeghiero, M., Roland, M., Rudd, D., Ryhti, K., Røjle Christensen, T., Sahoo,

https://doi.org/10.5194/egusphere-2026-4847
Preprint. Discussion started: 24 August 2026

G., Salze, P., Schaarup Sørensen, J., Schindler, D., Schlaipfer, M., Schmidt, M., Schmidt, P., Schmitt Oehler, M., Schrader, F., Segers, J., Shivhalli Gopal, A., Sibret, T., Siivola, E., Simioni, G., Sirca, C., Smith, P., Snellen, H., Sorgi, T., Soudani, K., Spano, D., Spence, K., Spyridakis, N., Stagakis, S., Staník, K., Staudinger, M., Stecher, M., Stellner, S., Stutz, T., Suopajärvi, S., Sutter, F., Taipale, R., Tallec, T., Tenca, F., Tezza, L., Thimonier Rickenmann, A., Thyrion, T., Tomelleri, E., Trotsiuk, V., Trusina, J., Tuittila, E.-S., Tuovinen, J.-P., Tyssandier, J., Vagnoli, C., Valay, J.-G., Van Damme, F., Van Look, J., Vande Sompele, A., Vandome, E., Varjonen, S., Vendrame, N., Ventura, M., Verbeeck, H., Vesala, T., Vescovo, L., Vincent, G., Vincke, C., Vitale, L., Vivaldo, G., Voisin, D., Vágner, L., Vähä, A., Waldner, P., Wiesen, R., Wilhelm, M., Winck, B., Yeung, K., Zaldei, A., Zampedri, R., Zawilski, B., Zenone, T., Zhao, H., Zhao, J., Zhu, J., Zimmermann, S., Zweifel, R., de Berranger, C., van Dijk, N., van der Molen, M., Šigut, L., and Šlížek, J.: Ecosystem final quality (L2) product in ETC-Archive format - release 2025-1, https://doi.org/10.18160/S6HM-CP8Q, iCOS Carbon Portal, 2025.

Running, S. W., Nemani, R. R., Heinsch, F. A., Zhao, M., Reeves, M., and Hashimoto, H.: A continuous satellite-derived measure of global terrestrial primary production, Bioscience, 54, 547–560, 2004.

Schlutow, M., Chew, R., and Göckede, M.: Spatial decomposition of eddy covariance fluxes: the FLUGS framework, https://doi.org/10.22541/au.176800032.22523770/v2, 2026.

Schmid, H.: Experimental design for flux measurements: matching scales of observations and fluxes, Agricultural and Forest Meteorology, 87, 179–200, 1997.

Schmid, H. P.: Source areas for scalars and scalar fluxes, Boundary-Layer Meteorology, 67, 293–318, https://doi.org/10.1007/BF00713146, 1994.

Subke, J.-A. and Bahn, M.: On the 'temperature sensitivity'of soil respiration: can we use the immeasurable to predict the unknown?, Soil Biology and Biochemistry, 42, 1653–1656, 2010.

Tramontana, G., Migliavacca, M., Jung, M., Reichstein, M., Keenan, T. F., Camps-Valls, G., Ogee, J., Verrelst, J., and Papale, D.: Partitioning net carbon dioxide fluxes into photosynthesis and respiration using neural networks, Global change biology, 26, 5235–5253, 2020.

Vesala, T., Kljun, N., Rannik, , Rinne, J., Sogachev, A., Markkanen, T., Sabelfeld, K., Foken, T., and Leclerc, M.: Flux and concentration footprint modelling: State of the art, Environmental Pollution, 152, 653–666, https://doi.org/10.1016/j.envpol.2007.06.070, 2008.

Xi, X., Yang, Q., Liu, C., Shupe, M. D., Han, B., Peng, S., Zhou, S., and Chen, D.: Evaluation of the Planetary Boundary Layer Height From ERA5 Reanalysis With MOSAiC Observations Over the Arctic Ocean, Journal of Geophysical Research: Atmospheres, 129, e2024JD040 779, https://doi.org/https://doi.org/10.1029/2024JD040779, e2024JD040779 2024JD040779, 2024.

Zanaga, D., Van De Kerchove, R., Daems, D., De Keersmaecker, W., Brockmann, C., Kirches, G., Wevers, J., Cartus, O., Santoro, M., Fritz, S., et al.: ESA WorldCover 10 m 2021 v200, 2022.

Zhu, S., Quaife, T., and Hill, T.: Uniform upscaling techniques for eddy covariance FLUXes (UFLUX), International Journal of Remote Sensing, 45, 1450–1476, 2024.

Zhuang, J., raphael dussin, Huard, D., Bourgault, P., Banihirwe, A., Raynaud, S., Malevich, B., Schupfner, M., Filipe, Levang, S., Gauthier, C., Jüling, A., Almansi, M., RichardScottOZ, RondeauG, Rasp, S., Smith, T. J., Stachelek, J., Plough, M., Pierre, Bell, R., Caneill, R., and Li, X.: pangeo-data/xESMF: v0.8.2, https://doi.org/10.5281/zenodo.8356796, 2023.